AD-A243 870

DTIC
ELECTE
JAN 0 6 1992
S
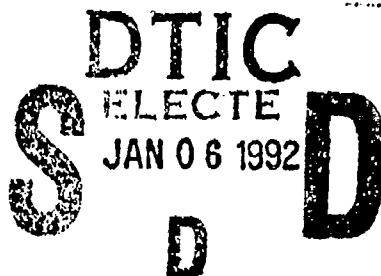D
D

DESIGN OF AN OPTIMUM THRUST NOZZLE

FOR A TYPICAL HYPERSONIC TRAJECTORY

THROUGH COMPUTATIONAL ANALYSIS

THESIS

David J. Herring
Captain, USAF

AFIT/GAE/ENY/91D-11

92-00053

92 1 2 062

DESIGN OF AN OPTIMUM THRUST NOZZLE FOR A TYPICAL

HYPERSONIC TRAJECTORY THROUGH COMPUTATIONAL ANALYSIS

THESIS

Presented to the Faculty of the School of Engineering

of the Air Force Institute of Technology

Air University

In Partial Fulfillment of the

Requirements for the Degree of

Master of Science in Aeronautical Engineering

David J. Herring

Captain, USAF

December 1991

Accesion For		
NTIS CRA&I		☑
DTIC TAB		[]
Unannounced		[]
Justification		
By		
Distribution /		
Availability Codes		
Dist	Avail and / or Special	
A-1		

Approved for public release; distribution unlimited

Acknowledgements

I wish to express my deepest gratitude to Captain John Doty for his seemingly infinite patience and knowledge in guiding me through this task. Had it not been for his invaluable ideas, timely suggestions, and wise counsel, this work would never have been completed. Additionally, I am very grateful to John Smith of the Aero Propulsion Laboratory, for taking the time to explain in great detail the intricacies as well as the 30 year history of the Scramjet cycle analysis program that I used to model nozzle internal flow conditions for this study.

On a more personal note, I would like to thank my sister Debra, my cousin Brian, and both of my parents, for their constant patience and support over the several months it took me to complete this most arduous task. They were always there for me, ready with words of encouragement on the many occasions when I became discouraged. In addition, I would also like to thank Robin Abb. Her positive outlook and refreshing sense of humor served to buoy my spirits at a time when the frustrations and anxieties seemed like they would never end. Finally, I would like to extend a special heartfelt thanks to Sarah Mendelsohn. Her words of advice and encouragement served to put this task into proper perspective, and carry me through a most difficult point in the writing process.

ii

Table of Contents

Table of Contents

Table of Contents

List of Figures

List of Figures

List of Figures

List of Tables

List of Symbols

a	speed of sound
a	first coefficient in equation for specific heat at constant pressure
A	area
acwl	cowl taper angle
b	term defined for Prandtl-Meyer angle
b	second coefficient in equation for specific heat at constant pressure
c	third coefficient in equation for specific heat at constant pressure
C_p	specific heat at constant pressure
C_v	specific heat at constant volume
C_v	combustion efficiency
c_1	first constant in equation for parabolic nozzle contour
c_2	second constant in equation for parabolic nozzle contour
c_3	third constant in equation for parabolic nozzle contour
d	fourth coefficient in equation for specific heat at constant pressure
dA	differential of area
dE	difference in E flux vector
dF	difference in F flux vector
e	specific internal energy
e	fifth coefficient in equation for specific heat at constant pressure
E	E flux vector

F	F flux vector
h	static enthalpy
h_{in}	nozzle inlet height
h_{ex}	nozzle exit height
hcwl	cowl thickness
L	nozzle length
M	Mach number
P	static pressure
q	dynamic pressure
r	nozzle circular arc radius of curvature
R_{gas}	gas constant for mixture
rucwl	upper cowl radius of curvature
T	static temperature
tcwl	cowl deflection angle
u	axial component of velocity, or constant convection velocity
v	normal component of velocity
V	velocity magnitude
x	axial direction
xcwl	cowl length
y	normal direction
z	coefficient for linearized approximate Riemann solver

GREEK SYMBOLS

β	difference between shock wave angle and flow deflection angle

γ	specific heat ratio
δ	flow turning angle
$\Delta\zeta$	axial step size in transformed coordinate system
ϵ	grid packing factor
ϵ	shock wave angle
ζ	transformed axial coordinate
η	transformed normal coordinate
η_x	partial derivative of transformed normal coordinate with respect to x
η_y	partial derivative of transformed normal coordinate with respect to y
η_c	combustion efficiency
η_{KD}	inlet process efficiency
η_{KE}	inlet kinetic energy efficiency
θ	flow angle
Λ	characteristic slope in transformed space
θ_B	nozzle circular arc attachment angle
ν	Prandtl-Meyer angle
ρ	density
σ	streamline slope
Ψ	general variable for Riemann problem

SUBSCRIPTS AND SUPERSCRIPTS

f, and fp	engine station designator corresponding to location of fuel injection, and location of flow freezing point, respectively

i	axial space direction index
i	numerical index
j	normal space direction index
j+1/2	Riemann node between grid points j and j+1
N	normal component
o	initial condition
T	tangential component
wave 1, 2, or 3	Riemann wave 1, 2, or 3, respectively
0, 2, and 3	engine station designator corresponding to inlet entrance, inlet exit, and combustor exit, respectively
0, 2, 4, or 6	Riemann region 0, 2, 4, or 6, respectively
1, 2	upstream or downstream of shock wave, respectively
1, 2, or 3	pertaining to Riemann wave 1, 2, or 3, respectively
+	positively biased information or positive split flux difference
-	negatively biased information or negative split flux difference

Abstract

An analysis of a planar supersonic nozzle for a NASP
type vehicle was performed with a computer program that used
the new upwind flux difference splitting (FDS) method.
Thrust optimization, off-design performance, and cowl angle
parametric analyses were accomplished, using the FDS code,
an oblique shock wave solver program, and a Scramjet cycle
analysis code, at six points on a 1000 psf maximum dynamic
pressure trajectory, for the Mach numbers 7.5, 10.0, 12.5,
15.0, 17.5, and 20.0. Results from the single parameter
optimization phase of the study indicated that for the Mach
number range from 7.5 to 20.0, the attachment angles
identified as optimum for the respective trajectory points
were 38.0, 38.6, 30.0, 24.6, 20.6, and 17.8. From this
range of angles, the 20.6 degree nozzle was found to produce
the minimum off-design performance losses over the entire
trajectory. This determination was based on selection
criteria biased toward the higher Mach numbers. Using the
20.6 degree nozzle attachment angle, a cowl angle parametric
analysis was performed to determine the extent to which off-
design performance losses could be recovered. Although this
study showed that cowl angles of 4.2, 2.6, 2.2, 3.1, 3.9,
and 4.3 degrees were required at the respective trajectory

points to maintain best recovery, nozzle performance was
shown to approach that of a variable geometry cowl for a
constant cowl deflection angle of 4.3 degrees. This study
also seemed to indicate that cowl use produced thrust
performance results which exceeded those of the single
parameter optimized nozzle.

DESIGN OF AN OPTIMUM THRUST NOZZLE FOR A TYPICAL HYPERSONIC TRAJECTORY THROUGH COMPUTATIONAL ANALYSIS

I   Introduction

1.1 Purpose

With the advent of the National Aero-Space Plane (NASP) program, significant government interest has been generated in the realm of design for hypersonic flight. An area that has been targeted for research is the hypersonic propulsion problem. Of its many facets, one aspect of this problem deserving attention is the design of an optimized supersonic nozzle (Doty, 1991:1). To date, very little research has been done in this field. One reason for this lack of knowledge is the relative paucity of convenient numerical methods available for use on complex flows containing numerous discontinuities (Doty, 1991:1). The purpose of this research is to use a new and efficient numerical technique to evaluate the design of maximum thrust planar supersonic nozzles (Doty, 1991:1), over a typical hypersonic trajectory for a transatmospheric vehicle such as the NASP (Doty, 1991:1). A secondary objective of this research is to conduct an off-design nozzle performance analysis and

1

cowl angle parametrics to determine the influence of cowl/external flow on nozzle performance (Doty, 1991:55).

1.2 Background

Design of supersonic nozzles presents many new challenges for the aeronautical engineer for many reasons. First, the hypersonic flight environment is an extremely hostile one. The extremes in temperature and thermal/mechanical stresses encountered in hypersonic flight present requirements that are at the limit of both material and cooling technology, and are thus very difficult to design for. The fact that such a vehicle must also maneuver and accelerate in this environment places even greater demands on the capabilities of the designer and modern technology. Also of importance is the fact that thrust production at hypersonic speeds presents demanding requirements. Conventional propulsion systems operating at hypersonic speeds do not behave the same way they do at subsonic or even supersonic speeds. At these higher speeds, when the air is diffused down to subsonic or near stagnation conditions for combustion, the resulting conversion of the air's kinetic energy to thermal energy can raise the temperature so high that little, if any, temperature rise occurs when fuel is added. This occurs because the normal combustion products of H_2O and CO_2 are strongly dissociated (Kerrebrock, 1981:252). Thus, instead of having the fuel's

2

chemical energy go toward accelerating the flow at the nozzle exit, it is used to further dissociate the combustion products. If the flow velocity at the nozzle exit does not increase, engine thrust will not increase, since thrust is proportional to exit velocity. This, of course, means there will be no useful thrust produced if the air is brought down to subsonic speeds for combustion. It is for this reason that thrust production at hypersonic speeds requires combustion at supersonic speeds, since diffusion to supersonic speeds provides a wider thermal margin that avoids the problem of dissociation. Thus, conventional engines are not feasible for flight in this speed regime, and must be replaced by supersonic combustion ramjet (Scramjet) engines.

According to Walton (1988:2), because of the extremely high Mach numbers that characterize flight in this speed regime, the resulting expansion at the afterbody can account for around 30% of the vehicle's thrust. For this reason, supersonic nozzles are not like conventional engine nozzles. Whereas conventional nozzles tend to be relatively small (as compared to the engine), and identifiable as discrete components at the aft end of the engine, Scramjet nozzles tend to be long and highly integrated with the airframe of the flight vehicle (Henry and Anderson, 1973). As illustrated in Figure 1, such a nozzle begins internally in

the engine, at the exit of the combustion chamber, and extends to include the vehicle afterbody as an expansion surface (Walton, 1988:2).

Another characteristic of these nozzles is the extreme sensitivity to changes in the parameters that govern performance. The limited research that has been done in this area indicates that even slight changes in ambient conditions can produce drastic changes in thrust performance. When it is considered that the best thrust performance that can be achieved from this kind of vehicle with current technology is just modestly better than enough to overcome vehicle drag, it becomes painfully clear that these slight changes in ambient conditions can result in loss of engine thrust or even loss of the vehicle (Billig, et al., 1990:118). It is clear there exists little or no margin for error in determining nozzle performance. Therefore, designing a nozzle for optimum performance is extremely important.

Related to the problem of too little margin for error, is the need for a hypersonic vehicle to fly within a prescribed envelope of altitude and flight speed as it transits the atmosphere. This is necessary so that certain flight and performance parameters can be maintained within useful limits as the vehicle carries out its mission. These parameters include such things as: dynamic pressure for

vehicle structural considerations; static temperature at the exit of the diffuser to maintain fuel autoignition (thus eliminating the need for flame holders); static temperature behind the bow shock for vehicle structural considerations; and static pressure in the diffuser exit for combustion chamber structural requirements. Of all these parameters, dynamic pressure is the only one that is exclusively a function of freestream conditions. For this reason, and because it represents a trajectory frequently encountered in the literature for a NASP type vehicle (Billig, 1987:119), this parameter was selected for the current study. Once selected, it was assumed that the vehicle traveled at this maximum q limit.

Here, the rationale is that not flying at the maximum q limit would represent a waste of design effort, technology, and money since the resulting vehicle would be structurally overdesigned, and thus stronger and consequently heavier than necessary. Overdesigning is a major problem because excess weight would necessitate a larger engine and more fuel. This would again further increase the vehicle weight in an upward spiral that could possibly result in a vehicle that is too heavy to fly. This is yet another example of how sensitive to small changes the design of this vehicle can be. This requirement to minimize weight while at the same time optimize performance further reinforces the need

for an optimized nozzle design. It is this need for an optimized supersonic nozzle that is the motivating force behind this study. What remains is the employment of an effective method for performing this optimization.

1.3 Method of Analysis

The technique and computer program recently implemented by Doty (1991) for the determination of maximum thrust planar nozzles in an inviscid, supersonic, rotational, adiabatic steady flow provided the means for accomplishing this study. Prior to the implementation of this new technique, the analysis and design of supersonic nozzles was a formidable task. The primary reasons for this relate to the fact that there are few numerical codes that can efficiently produce accurate solutions to the complicated flowfields present in the nozzles (see Figure 2) of NASP type vehicles (Doty, 1991:2). These flowfields require solution methods able to accurately calculate flows with strong property gradients without producing numerical oscillations (Doty, 1991:1). Additionally, these methods must also be capable of handling the interaction of shock waves, expansion waves, and contact surfaces in the solution procedure. The few numerical codes that do exist that can accomplish this task are extremely time consuming and costly to use (Doty, 1991:1), and are therefore not desirable for an optimization procedure which may require the entire

flowfield be analyzed several times. Now, with the
development of this new technique, it is possible to produce
realistic trends in nozzle performance and design for high
speed vehicles with significant savings in computational
time (Doty, 1991:1).

What has made it practical to perform the here-to-fore
extremely difficult and costly task of nozzle performance
trend analysis and design a nozzle for a hypersonic vehicle,
is the Flux-Difference-Split (FDS) method. As implemented
for this research, this is a robust, first-order accurate
FDS method that is as accurate as most second-order finite
difference methods (Taylor et al., 1972, Peyret et al.,
1983), and is an integral part of this new technique. By
itself, this method provides an approach for capturing the
complicated physics of the flowfield (Doty, 1991:2). But
with the employment of the steady planar form of the Euler
equations as the basis for its flowfield model,
computational efficiency is greatly increased using this
technique. The basis for the FDS method is the solution of
the Riemann problem, and it is with the solution of the
Riemann problem that the application of the FDS method
becomes a very straight forward process. Thus, this new
technique for the analysis of supersonic nozzles is
possible.

Airframe
Integrated
Nozzle
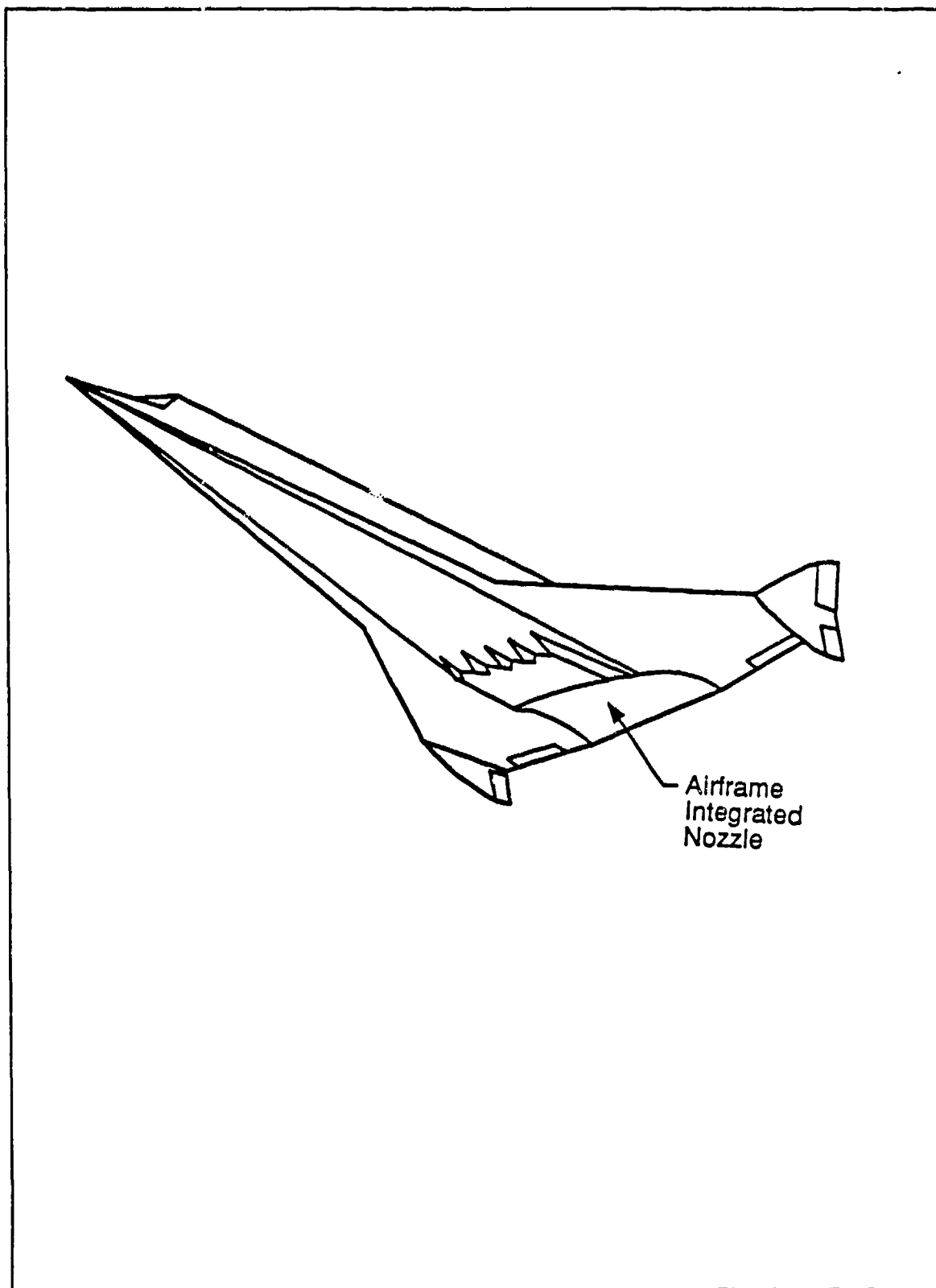
Figure 1. Typical Hypersonic Vehicle. (Doty, 1991, 4)
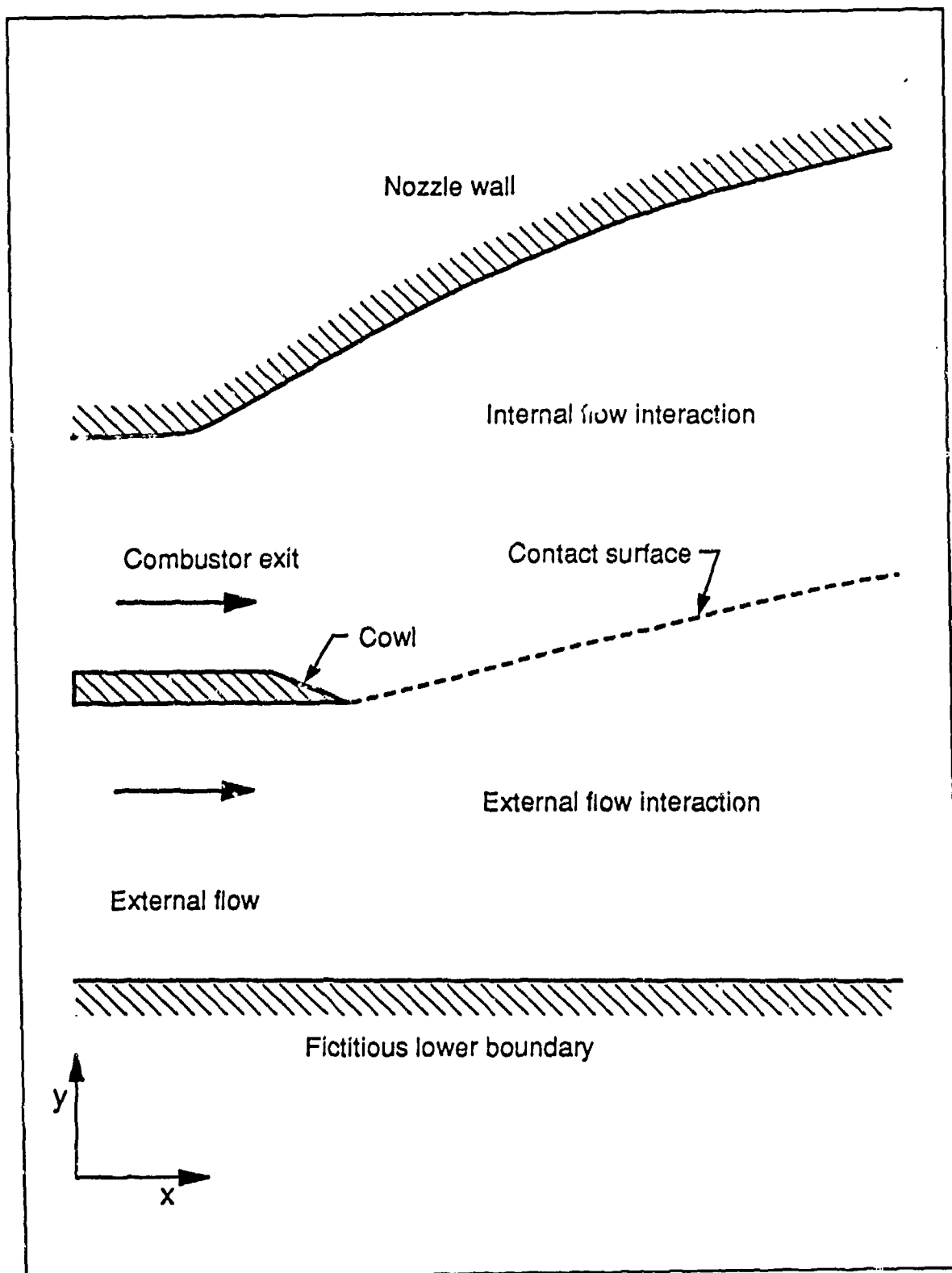
Figure 2. Internal and External Nozzle Flow and Geometry. (Doty, 1991: 5)

9

II Analytical Development

2.1 Governing Equations (Doty, 1991:Ch 2)

For the planar, steady, adiabatic, inviscid flow of a compressible fluid with no external work or body forces, the Euler equations, given in vector divergence form, govern the fluid flow:

$$\frac{\partial \mathbf{E}}{\partial x} + \frac{\partial \mathbf{F}}{\partial y} = 0 \qquad (1)$$

where the **E** and **F** vectors are written in terms of the conservation variables as

$$\mathbf{E} = \begin{bmatrix} \rho u \\ \rho u^2 + P \\ \rho u v \\ u(\rho e + P) \end{bmatrix} \qquad \mathbf{F} = \begin{bmatrix} \rho v \\ \rho v u \\ \rho v^2 + P \\ v(\rho e + P) \end{bmatrix} \qquad (2)$$

The first of Eqs (2) is the continuity equation, the second and third are the axial and normal momentum equations, respectively, and the fourth is the energy equation.

2.1.1 Thermodynamic Model

The equations of state chosen for this study are those of a thermally and calorically perfect gas. The equation of state for a thermally perfect gas is given by:

$$T = \frac{P}{\rho R} \qquad (3)$$

while for a calorically perfect gas the total specific
internal energy is given by:

$$\rho e = \frac{P}{\gamma - 1} + \frac{1}{2}\rho(u^2 + v^2) \qquad (4)$$

2.2 The Trajectory

As stated in Section 1.2, a hypersonic vehicle is
usually analyzed along a pre-defined flight profile as it
transits the atmosphere. This is necessary so that certain
flight and performance parameters can be maintained within
useful limits. For this study a maximum dynamic pressure,
q, trajectory was chosen, with 1000 psf used as the q limit
that the trajectory was based on. This type of trajectory
was chosen because, given the fact that no specific vehicle
characteristics or mission requirements were identified, it
served to define a useful schedule of altitudes and flight
speeds without unnecessarily increasing the complexity of
the analysis. Although 1000 psf was chosen somewhat
arbitrarily, this value was selected because it represented
one of the trajectories more frequently encountered in the
literature for a NASP type vehicle (Billig, 1987:119).

11

With the vehicle q limit established, determination of
the flight trajectory became a matter of applying the
equations for dynamic pressure

$$q = \frac{1}{2} \rho V^2 \tag{5}$$

and the speed of sound in a perfect gas

$$a^2 = \frac{P\gamma}{\rho} \quad or \quad a^2 = \gamma RT \tag{6}$$

The state equation for a thermally perfect gas, Eq (3),
is used to derive an equation that expresses static pressure
as a function of dynamic pressure, specific heat ratio, and
Mach number. This expression results from solving the
dynamic pressure equation for velocity

$$V^2 = \frac{2q}{\rho} \tag{7}$$

and dividing the subsequent equation by the speed of sound
equation. This results in an expression in terms of Mach
number, given by:

$$M^2 = \frac{V^2}{a^2} = \frac{V^2}{\gamma RT} = \frac{2q/\rho}{\gamma RT} \tag{8}$$

12

Finally, Eq (9) is arrived at by substituting for density into this new expression using Eq (3), the equation for a thermally perfect gas.

$$P = \frac{2q}{\gamma M^2} \qquad (9)$$

Determination of the other freestream conditions from Mach number information was facilitated through the use of the equations that defined the 1962 Standard Atmosphere Tables (US COESA, 1962:4-16). This procedure started with choosing a Mach number and then using Eq (9) to determine the corresponding static pressure for a given q, and with γ assumed constant and equal to 1.4. The pressure equation from the Standard Atmosphere was then solved for altitude using this value for pressure from Eq (9). Once altitude was determined, all of the other freestream conditions became readily available from the remaining atmosphere equations. A plot of the flight profile that results from application of this procedure is presented in Figure 3. Details of the freestream conditions determined from Standard Atmosphere equations are contained in Table 1.

2.3 The Riemann Problem and Its Solutions (Doty, 1991:Ch 3)

The Riemann problem, the solution of a discontinuity, provides the basis for the flux-difference-split (FDS) method. The wave-like nature of the Riemann problem is used

13

to split the solution to the Riemann problem along the preferred paths of information propagation. In this manner, discontinuities such as shock waves are processed and the resulting information is used to calculate the numerical solution.

Although both first-order and second-order accurate FDS methods exist, the first-order accurate method was chosen for this investigation. This selection was made for two reasons. First, because the first-order accurate method behaves monotonically, it is very robust. It has been shown that this monotonic behavior of the numerical solution is extremely important (van Leer, 1973) in regions where strong property gradients exist, such as near shock waves and contact surfaces. The use of second-order accurate conservative, monotonic difference schemes (van Leer, 1973, 1974, 1977a, 1977b) becomes extremely cumbersome because they require special treatment near boundaries and in regions of strong property gradients. Second, the first-order FDS method is very accurate. Based on the Godunov initial value Riemann problem, this scheme has been demonstrated to be as accurate as many second-order accurate finite difference schemes (Taylor et al., 1972, Peyret et al., 1983). Comparison of first-order accurate FDS results with exact solutions and other second-order accurate methods bears this out (Doty, 1991:8).

2.3.1 The Riemann Problem

The representation of the Riemann problem is illustrated in Figure 4. The general flow property, Ψ, has an arbitrary spatial distribution represented by the solid line. These general flow properties are modeled as a series of uniform flow regions (Godunov, 1959). The dashed line represents these regions of uniform flow at each of the nodes, with the discontinuity assumed to occur half-way between the nodes.

Collapse of the discontinuity produces the possible pattern of waves shown in Figure 5. Wave (3), referred to as the positive wave because it normally carries information in the positive y direction, may be a compression (perhaps shock) or expansion depending on the particular flowfield under investigation. Wave (2) is the contact surface that separates the Riemann regions. Wave (1) is referred to as the negative wave because it normally carries information in the negative y direction. Similar to wave (3), wave (1) may be a compression (perhaps shock) or expansion. The possibility also exists that both waves (3) and (1) will be compressions or both expansions. The notation for the Riemann problem between grid points j and j+1 in Figure 5 is as follows:

Riemann region 6 = known values at grid point "j+1"
Riemann region 4 = unknown values at mid point "j+1/2"
Riemann region 2 = unknown values at mid point "j+1/2"

15

Riemann region 0 = known values at grid point "j"

Similar notation exists for other pairs of grid points, simply by permuting the indices.

2.3.2 <u>Solution to the Riemann Problem</u>

The solution to the Riemann problem provides the numerical fluxes in the regions 2 and 4, Figure 5. The Riemann problem for planar, supersonic flow may be solved by any one of three different methods. The first method solves the Riemann problem exactly, and is therefore the most computationally intensive. It solves the general case where the possible compression wave is a shock wave. The second method solves the Riemann problem approximately by assuming that the shock wave is an isentropic compression (Osher, 1981). This approximate solution thereby replaces the shock wave by a Prandtl-Meyer compression. The third method solves the approximate Riemann problem approximately by linearizing the Prandtl-Meyer relations (Pandolfi, 1985). The FDS method solves the Riemann problem using one of these methods, thereby incorporating solutions to discontinuous flows; it then splits this solution and sends the information in the correct direction.

2.3.2.1 Exact Solution

The exact solution to the Riemann problem requires the iterative solution of coupled nonlinear shock-wave/contact-surface/expansion-wave relations. The shock jump relations and the Prandtl-Meyer equations must be solved simultaneously because waves (1) and (3) are coupled by the contact surface, wave (2).

In addition to the solution of the coupled sets of equations, the equations governing the shock wave and Prandtl-Meyer wave are highly nonlinear and require iterative techniques. One possibility for the pattern of waves illustrated in Figure 5 is that wave (1) is a shock wave and wave (3) is an expansion wave. For the shock wave, upstream properties are known in region 0 and the solution is sought in region 2. The nonlinear equation relating the flow turning angle, δ to the shock wave angle, ε is given by:

$$\frac{1}{\tan\delta} = \left(\frac{\gamma+1}{2} \frac{M_1^2}{M_1^2\sin^2\varepsilon - 1} - 1 \right) \tan\varepsilon \qquad \textbf{(10)}$$

(Zucrow and Hoffman, 1976:360). This equation must be iterated for the shock wave angle for a known amount of flow turning.

Similarly, the expansion wave upstream properties are known in region 6 and the solution is sought in region 4.

17

The nonlinear equation to be solved in this instance is the Prandtl- Meyer relation, which is given by:

$$v_4 = b \arctan\left[\frac{1}{b}\sqrt{M_4^2-1}\right] - \arctan\left[\sqrt{M_4^2-1}\right] \qquad (11)$$

where

$$b \equiv \sqrt{\frac{\gamma+1}{\gamma-1}} \qquad (12)$$

Eq (11) must be solved iteratively for the Mach number given the Prandtl-Meyer angle in region 4.

In addition to the iterations required for the shock and expansion waves, the flow angle and static pressure in regions 2 and 4 must match across the contact surface, wave (2). This secondary iteration procedure may require several trials before the exact solution to the Riemann problem at each node pair is solved.

2.3.2.2 Approximate Solution

For the approximate solution to the planar Riemann problem, all compression waves are treated as isentropic (even though they may be shock waves). For the case where wave (1) is a compression and wave (3) is an expansion, both waves are calculated using Prandtl-Meyer relations. The

compression and expansion solutions are again coupled by virtue of the contact surface, wave (2).

For the compression wave, the solution to the nonlinear Prandtl-Meyer equation requires iteration for the Mach number in region 2, M_2. This is accomplished using a relationship given by:

$$v_2 = b \arctan\left[\frac{1}{b}\sqrt{M_2^2-1}\right] - \arctan\left[\sqrt{M_2^2-1}\right] \qquad (13)$$

For the expansion wave, the solution to the nonlinear Prandtl-Meyer equation requires iteration for the Mach number in region 4, M_4, as outlined by Eq (11). In the same fashion as the exact Riemann problem, the approximate solution requires that the slope and static pressure across the contact surface match, involving an additional iteration procedure.

2.3.2.3 Linearized-Approximate Solution

The linearized approximate solution eliminates all of the iteration required for the exact and the approximate Riemann solutions. Similar to the approximate solution, the compressions are treated as isentropic. The resulting set of Prandtl-Meyer relations are then linearized to produce a set of algebraic equations which can be solved in closed form. For the case where wave (1) is a compression, the relevant, linearized Prandtl-Meyer relation is given by:

19

$$[\ln(P)]_2 + (z_o)\sigma_2 = [\ln(P)]_o + (z_o)\sigma_o \qquad \textbf{(14)}$$

where

$$z \equiv \frac{(\gamma u^2/a^2)}{\sqrt{M^2-1}} \qquad \textbf{(15)}$$

Similarly, the linearized Prandtl-Meyer relation required when wave (3) is an expansion wave is given by:

$$[\ln(P)]_4 - (z_6)\sigma_4 = [\ln(P)]_6 - (z_6)\sigma_6 \qquad \textbf{(16)}$$

After the Riemann problem has been solved by any of the methods described above, the calculation of the Riemann fluxes and flux differences across the waves is performed. The splitting of these flux differences provides the information required for the numerical solution. Detailed information on each of these three solution methods, along with details of the procedures relating to the splitting of the flux differences, is contained in Doty, 1991: 160-198. A stencil for a multiple point Riemann problem is illustrated in Figure 6. For reasons of speed, and convenience, while maintaining suitable accuracy (Doty, 1991: 33), the linearized-approximate solution method was used exclusively for the purposes of this investigation.

2.5 The Flux-Difference-Split Method

Once the Riemann problem (described above) is solved, the information resulting from this solution is used to form the Riemann fluxes. It is from these fluxes that the flux differences are calculated. These flux differences are, in turn, split to form the numerical contributions which are used in the computational algorithm (Doty, 1991: 177). What follows is a very brief description of this process, along with a listing of the numerical algorithm used to advance the solution to the next downstream plane.

2.5.1 Riemann Fluxes and Flux-Differencing
(Doty, 1991:Sec J.1)

The solution to the Riemann problem provides the basis for the calculation of the Riemann fluxes in regions 0, 2, 4, and 6 in Figure 5 at each half node ($\ldots$, $j-1/2$, $j+1/2$, $\ldots$). The divergence form of vectors **E** and **F** is presented in Eq (2) and repeated here for convenience:

$$
\boldsymbol{E} = \begin{bmatrix} \rho u \\ \rho u^2 + P \\ \rho uv \\ u(\rho e + P) \end{bmatrix} \qquad \boldsymbol{F} = \begin{bmatrix} \rho v \\ \rho vu \\ \rho v^2 + P \\ v(\rho e + P) \end{bmatrix} \qquad \textbf{(2)}
$$

The Riemann fluxes are calculated for each of the components of the **E** and **F** vectors. For example, the first component of the **E** vector (E1) from Eq (2) is ρu. The flux

21

component E1 is evaluated in the Riemann regions 0, 2, 4, and 6 as:

$$(E1)_0 = \rho_0 u_0 \qquad (17)$$

$$(E1)_2 = \rho_2 u_2 \qquad (18)$$

$$(E1)_4 = \rho_4 u_4 \qquad (19)$$

$$(E1)_6 = \rho_6 u_6 \qquad (20)$$

Similar calculations are performed for the remaining **E** vector components, as well as for those of the **F** vector in preparation for the evaluating the flux differences.

With reference to Figure 5, the flux differences across waves 1, 2, and 3 are calculated by forming the differences of the Riemann fluxes. For example, the differences of the Riemann fluxes for the first component of the **E** vector (dE1) across waves 3, 2, and 1, respectively, are simply:

$$(dE1)_{wave3} = (E1)_6 - (E1)_4 = \rho_6 u_6 - \rho_4 u_4 \qquad (21)$$

$$(dE1)_{wave2} = (E1)_4 - (E1)_2 = \rho_4 u_4 - \rho_2 u_2 \qquad (22)$$

$$(dE1)_{wave1} = (E1)_2 - (E1)_0 = \rho_2 u_2 - \rho_0 u_0 \qquad (23)$$

22

Summing the contributions of the flux differences
across the waves from Eqs (21), (22), and (23) gives the
total contribution at Riemann node j+1/2:

$$(dE1)_{j+1/2} = [(dE1)_{wave3} + (dE1)_{wave2} + (dE1)_{wave1}]_{j+1/2} \quad \textbf{(24)}$$

Substituting Eqs (21), (22), and (23) into Eq (24) and
recalling that Riemann nodes 6 and 0 correspond to nodes j+1
and j, respectively, yields the equivalent finite difference
representation:

$$(dE1)_{j+1/2} = (E1)_6 - (E1)_0 = (E1)_{j+1} - (E1)_j \quad \textbf{(25)}$$

Rather than use the total contribution of the flux
differences, the flux-difference-split (FDS) approach
attempts to utilize the wave-like nature of the supersonic
flow to send the flux differences in the correct physical
direction.

2.5.2 Splitting the Flux Differences (Doty, 1991: Sec J.2)

The information is known at plane i, node j in Figure 6
and the solution is sought at plane i+1, node j. A solution
is obtained at plane i+1, node j, by using the differenced
fluxes to carry this information to the next node location.
However, not all of this information is transmitted. As
mentioned above, information is only transmitted in the

direction that matches the correct physics of the flow at the node location.

In steady, two-dimensional flow, the splitting of the flux differences is accomplished for the Riemann nodes by calculating the slope of the waves and employing a splitting operator. For example, using Chakravarthy's notation at Riemann node j-1/2, the positive split flux difference across wave 1 for the **E** vector is:

$$\{d\mathbf{E}_{j-1/2}^{wave1}\}^+ = \{\max[sign(\Lambda_1),0.0]\,[\mathbf{E}_2 - \mathbf{E}_0]\}_{j-1/2} \qquad (26)$$

where Λ_1 is the slope of wave 1. If the sign of Λ_1 is negative, the sign operator selects:

$$sign(\Lambda_1) = -1 \qquad (27)$$

Then the max operator chooses:

$$\max(-1,0.0) = 0.0 \qquad (28)$$

Therefore, the multiplier for the flux difference $[\mathbf{E}_2-\mathbf{E}_0]$ is zero, and there will be no positive-split flux difference from node j-1/2 for wave1. On the other hand, if the sign of Λ_1 is positive, the flux difference multiplier is unity. In this fashion, the flux differences are split into positive and negative contributions, for each wave

24

(i.e., 3, 2, and 1), at each Riemann node (i.e., ...,j-1/2, j+1/2,...), for both the **E** and **F** vectors.

Summing the positive and negative contributions for all the waves at Riemann nodes j+1/2 and j-1/2 yields the numerical fluxes. For the **E** vector, this procedure yields:

$$dE^-_{j+1/2} = \{dE^{wave3}_{j+1/2}\}^- + \{dE^{wave2}_{j+1/2}\}^- + \{dE^{wave1}_{j+1/2}\}^- \qquad (29)$$

$$dE^+_{j-1/2} = \{dE^{wave3}_{j-1/2}\}^+ + \{dE^{wave2}_{j-1/2}\}^+ + \{dE^{wave1}_{j-1/2}\}^+ \qquad (30)$$

The identical procedure for the **F** vector yields a similar result.

With the Riemann problem solved, the Riemann fluxes calculated, the flux differences formed and split, and the numerical fluxes determined, the only remaining operation to perform is that of advancing or marching the solution from plane i to i+1. This final operation is performed using the FDS numerical algorithm.

2.5.3   First-Order Accurate Flux-Difference-Split
         Numerical Algorithm for an Interior Point
         (Doty, 1991: Sec 3.3)

The first order accurate FDS solution to the transformed governing equations uses the biased information just adjacent to the node j where the solution is required. For example, from Figure 6, the negatively biased information from Riemann node j+1/2 (above j) is used while

25

the positively biased information from Riemann node j-1/2
(below j) is used. Thus, the first-order accurate FDS
method for an interior point is:

$$E_j^{i+1} = E_j^i - \Delta\zeta\eta_x \left(dE_{j-1/2}^+ + dE_{j+1/2}^-\right) - \Delta\zeta\eta_y \left(dF_{j-1/2}^+ + dF_{j+1/2}^-\right) \quad (31)$$

Here $\Delta\zeta$ is the step size, which is determined from the
stability criterion. The transformation metrics, η_x and η_y,
shown in this equation are evaluated using the computational
coordinates ζ and η. Thus with initial values for all nodes
at plane i known, and a solution sought for node j at the
next downstream plane at i+1, it is now possible to solve
for the unknowns at the new location using the relationships
expressed in equation (31). More complete details of this
solution procedure are given in Doty, 1991: Appendix K.
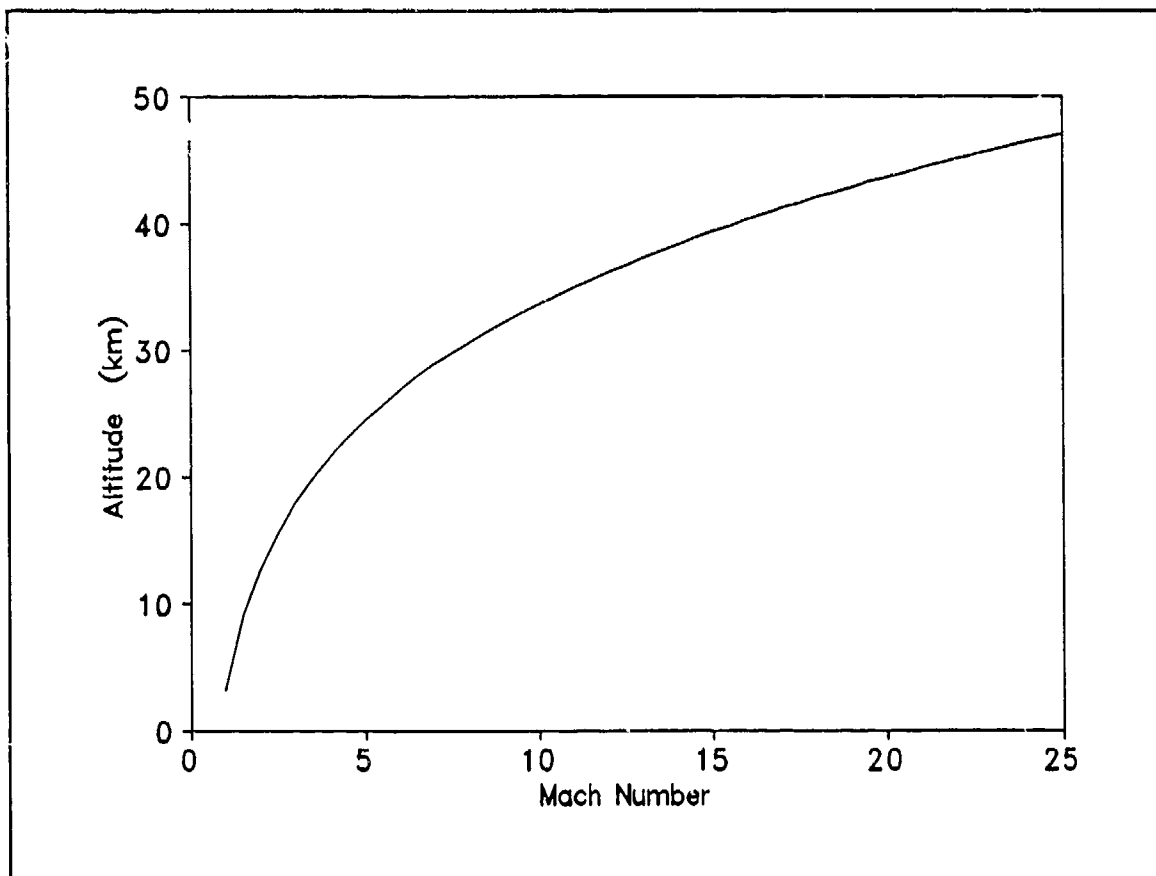
Figure 3.   The Relationship Between Altitude and Mach Number
for a 1000 psf Constant "q" Trajectory
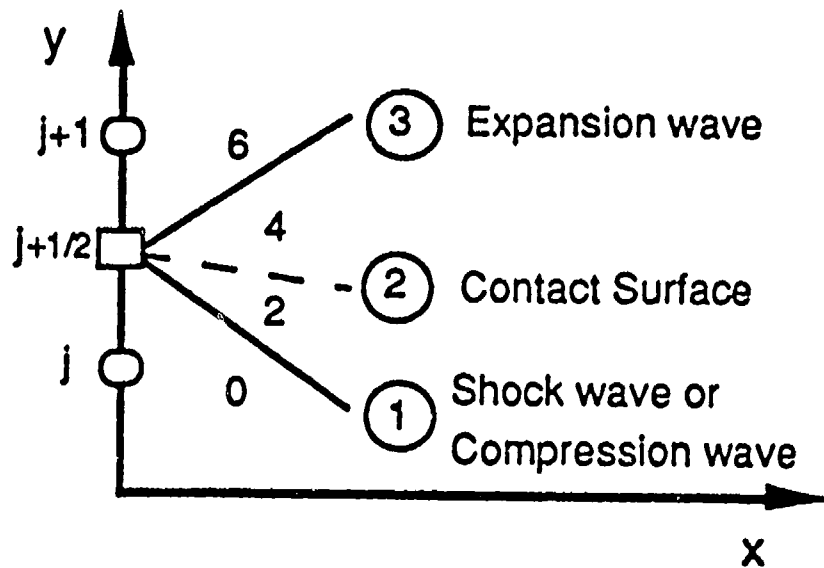
Figure 4. General property distribution (Doty, 1991:14).
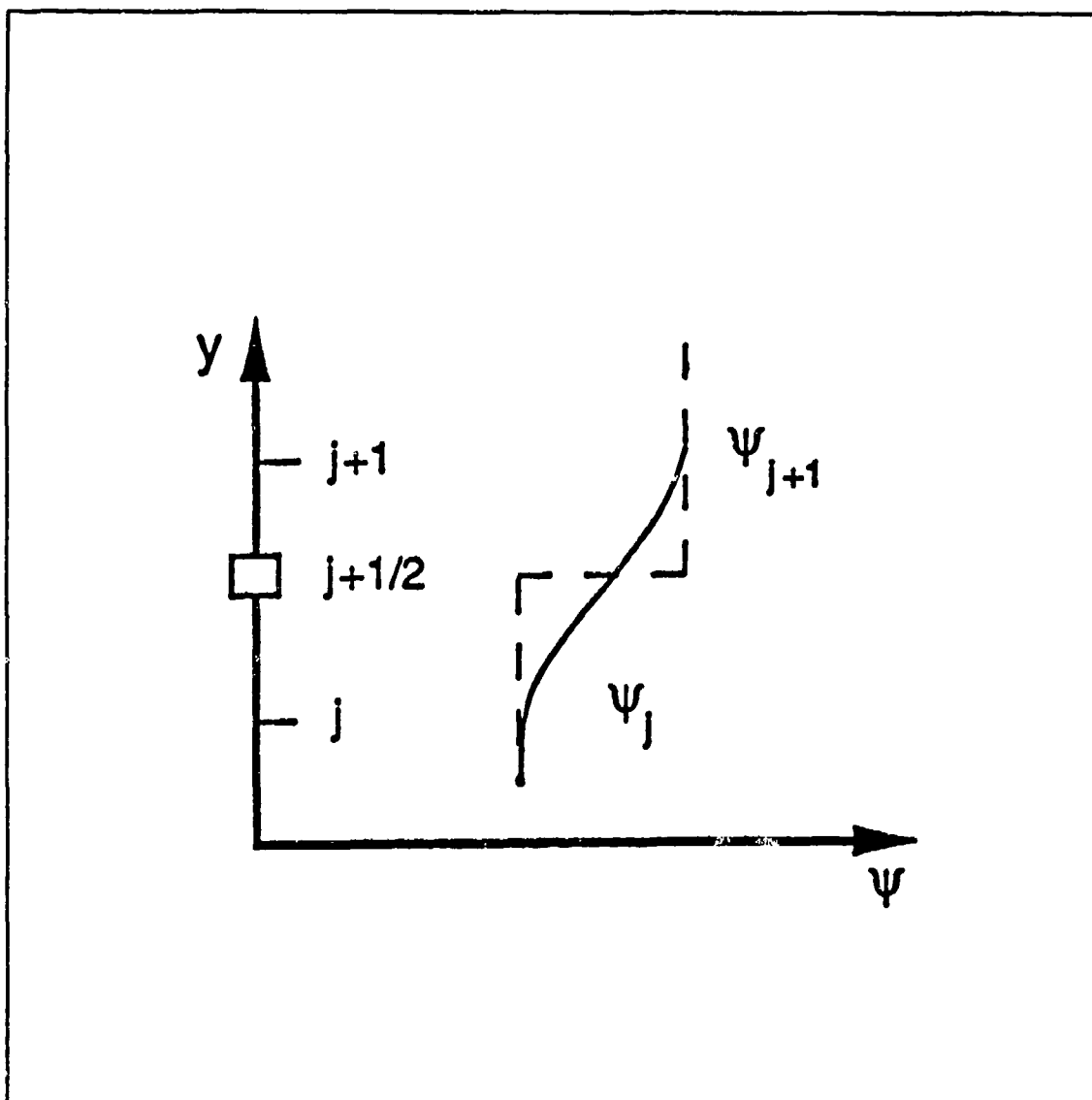
Figure 5. Riemann description for planar flow
(Doty, 1991:14).
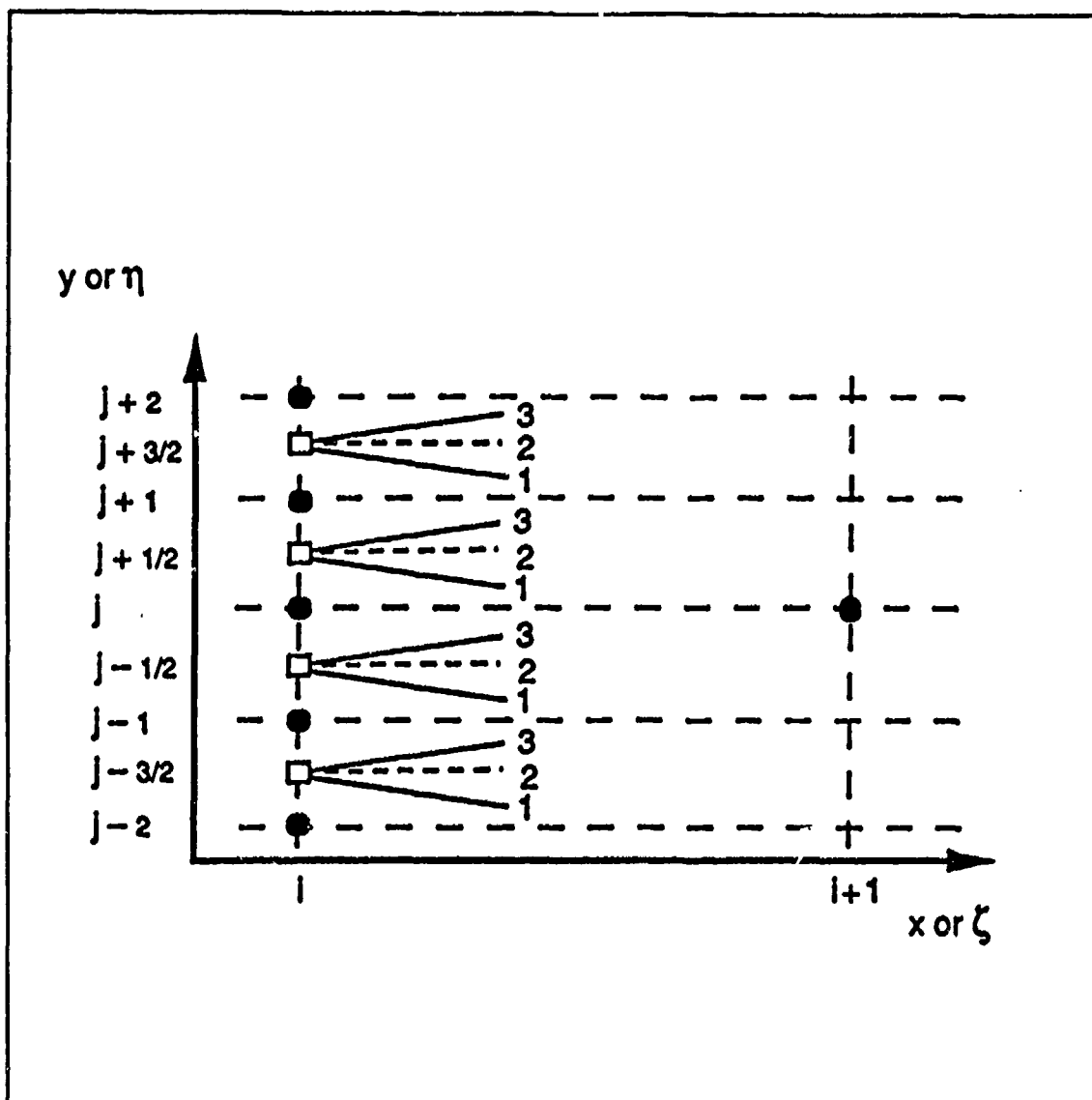
Figure 6. Multiple point Riemann stencil (Doty, 1991:14).

Table 1.   Freestream flow conditions at each trajectory point.

Freestream parameter	Value		
Mach number	7.5	10.0	12.5
altitude, (km)	29.896	33.791	36.928
static pressure, P (N/m²)	1216.01	684.00	437.76
static temperature, T (°K)	226.4	233.2	241.8
density, ρ (kg/m³)	0.018711	0.010220	0.006306
velocity magnitude, V (m/s)	2262.4	3061.2	3897.1
specific heat ratio, γ	1.4	1.4	1.4
gas constant, R_{gas} (J/kg/°K)	287.0	287.0	287.0

Freestream parameter	Value		
Mach number	15.0	17.5	20.0
altitude, (km)	39.581	41.887	43.934
static pressure, P (N/m²)	304.00	223.35	171.00
static temperature, T (°K)	249.2	255.6	261.2
density, ρ (kg/m³)	0.004250	0.003045	0.002281
velocity magnitude, V (m/s)	4746.9	5608.5	6480.2
specific heat ratio, γ	1.4	1.4	1.4
gas constant, R_{gas} (J/kg/°K)	287.0	287.0	287.0

III Preliminary Procedures

3.1 Introduction

Procedures followed in preparing for and actually performing the nozzle thrust analysis and optimization are presented in this chapter. The methods used to determine external and internal flow properties are described, along with the computer programs that actually performed the computations. The manner in which the FDS program was used to determine thrust performance data is also presented. Finally, the methods used to perform the nozzle optimization and cowl off-design parametric analysis are also described.

3.2 External Flow

Since a major aspect of this research was to investigate the influence of external flow on nozzle performance, it was necessary to determine external flow conditions for each point on the trajectory. With the modeling of the external flow region as that on the downstream side of an oblique shock wave, initially this determination seemed be a simple matter of solving the oblique shock wave problem for a perfect gas. However, due to the large temperature variation associated with the hypersonic Mach numbers examined in this study, a perfect gas model was deemed inappropriate (van Wie, et al., 1990:101). To attain the most accurate approximation

32

possible of the underbody compression without knowing much
about vehicle geometry, a calorically imperfect, but
thermally perfect gas model was substituted. This also
allowed the external flow calculations to remain consistent
with the model for internal flow calculations (to be
discussed later). This assumption furnished a reasonable
approximation for the compression, while realistically
modeling caloric behavior. Unfortunately, with this
requirement solution of the oblique shock wave problem was
no longer trivial; the solution now involved several
iterative schemes to account for the effect of variable
caloric behavior on flow properties. What follows is a
description of the iterative method used and computer
program developed to solve the oblique shock wave problem
for an imperfect gas at each point on the trajectory.
Detailed information on the equations used to model caloric
behavior is contained in Zucrow and Hoffman, 1976: 53-63.

3.2.1   The Caloric Model for Air

In this phase of the study, air in the external flow
region (see Figure 2), was assumed to be comprised of the
three constituents nitrogen, oxygen, and argon in the
respective molar percentages of 78.11, 20.96, and 0.93
(Zucrow and Hoffman, 1976:58). Caloric behavior for air was
modeled using the following two equations:

$$h = \left(h_o + aT + \frac{bT^2}{2} + \frac{cT^3}{3} + \frac{dT^4}{4} + \frac{eT^5}{5} \right) R \qquad (32)$$

for static enthalpy (mole basis), and

$$C_p = (a + bT + cT^2 + dT^3 + eT^4) R \qquad (33)$$

for specific heat at constant pressure. In these equations a, b, c, d, e, and h_o are constants that are exclusive to the gas being modeled (Gordon, McBride 1971). Specific heat at constant volume and the specific heat ratio were determined from the following two respective relationships:

$$C_v = C_p - R \qquad (34)$$

$$\gamma = \frac{C_p}{C_v} \qquad (35)$$

What follows is a description of the iterative procedure that used these equations to solve the oblique shock wave problem.

3.2.2   Iterative Solution of The Oblique Shock Wave Problem (Zucrow and Hoffman, 1976:Sec 7.8)

An important aspect of supersonic nozzle behavior is the interaction between the flow that travels along the undersurface of the vehicle (external flow), and the flow

34

issued from the exit of the combustor (internal flow).
Since, for the purposes of this study, the external flow was
modeled as that on the downstream side of the oblique shock
wave formed off the nose of the vehicle, it was necessary to
solve the oblique shock wave problem.

Figure 7 illustrates the example of an oblique shock
wave that is produced by a hypersonic vehicle. The
requirement for the iterative method employed here for
solution of this shock wave problem results for several
reasons. First, as stated earlier, due to the magnitude of
the static temperature rise across an oblique shock wave at
hypersonic speeds, the equations for a perfect gas no longer
apply (Zucrow and Hoffman, 1976:Sec 4.5). However, although
there is an equation that relates static temperature to
enthalpy, the nonlinear relationship between these two
quantities cannot be explicitly expressed when temperature
is the unknown. Second, the equations that relate upstream
static pressure and enthalpy are coupled in a nonlinear
manner through the density. And finally, the system of
equations is indeterminate, since there are more unknowns
than there are equations to solve for them. For these
reasons the following procedural steps were used to solve
the oblique shock wave problem for this study.

1.   Initial flow conditions of pressure P_1, temperature T_1,
     density ρ_1, enthalpy h_1, and velocity V_1 are determined

in region 1 (see Figure 7) from the freestream properties on the trajectory.

2. With the initial flow conditions established, a trial value for ε, the oblique shock wave angle, is then assumed. For a first guess the perfect gas oblique shock wave solution is used. This value is determined by solving Eq (10), the nonlinear equation relating flow turning angle, δ, to the shock wave angle, ε,

$$\frac{1}{\tan\delta} = \left(\frac{\gamma+1}{2} \frac{M_1^2}{M_1^2\sin^2\varepsilon -1} -1 \right) \tan\varepsilon \qquad (10)$$

3. The newly established value for ε is next used to determine a value for M'_1, where this quantity is defined as:

$$M'_1 = M_1\sin\varepsilon \qquad (36)$$

The trial value for ε is also used to calculate the normal and tangential components (relative to the shock wave) of the freestream velocity V_{N1} and V_{T1}, using

$$V_{N1} = V_1\sin\varepsilon \qquad (37)$$

and

$$V_{T1} = V_T = V_1\cos\varepsilon \qquad (38)$$

4. Next, a trial value for ρ_2, the density on the downstream side of the oblique shock wave, is assumed. For a first guess the perfect gas flow property relation for normal shocks

$$\frac{\rho_2}{\rho_1} = \frac{V_1}{V_2} = \frac{(\gamma + 1) M_1'^2}{2 + (\gamma - 1) M_1'^2} \qquad (39)$$

and M_1' are used for this determination.

5. With density information established, values for pressure and enthalpy on the downstream side of the oblique shock wave, P_2 and h_2, are calculated using

$$P_2 = P_1 + \rho_1 V_{N1}^2 \left(1 - \frac{\rho_1}{\rho_2}\right) \qquad (40)$$

$$h_2 = h_1 + \frac{V_{N1}^2}{2} \left[1 - \left(\frac{\rho_1}{\rho_2}\right)^2\right] \qquad (41)$$

6. Next, a new value for T_2 is determined from the value for h_2 established in step 5 above by iterating on Eq (32) using a numerical solution technique such as the Newton-Raphson method.

7. This new value for T_2, is next used along with P_2 from step 5, and Eq (3) to determine a new value for ρ_2.

8. If this new value for ρ_2 is within the specified tolerance of the value originally assumed in step 2, this portion of the solution has been completed. If the agreement is unsatisfactory, steps 5 to 8 are then repeated using this new value for ρ_2 until convergence is obtained.

9. Once convergence on ρ_2 is achieved, V_2 is then calculated using

$$V_{N2} = \frac{\rho_1 V_{N1}}{\rho_2} \qquad (42)$$

and

37

$$V_2 = \left(V_T^2 + V_{N2}^2 \right)^{1/2} \qquad\qquad\qquad \textbf{(43)}$$

Using V_2 and

$$\varepsilon = \delta + \sin^{-1}\left(\frac{V_{N2}}{V_2} \right) \qquad\qquad\qquad \textbf{(44)}$$

a new value for ε is obtained. If this new value is within the specified tolerance of the previous value for ε, then the solution is complete. If the agreement is unsatisfactory. steps 2 to 9 are repeated with the new ε until satisfactory convergence is obtained.

10. Once convergence on ε is obtained, the final values for flow conditions on the downstream side of the oblique shock wave are calculated using the procedures described in steps 5, 6, and 7, and equations (3), (6), (32), (33), (34), (35), (40), and (41).

If convergence is not achieved immediately in the various iteration steps (as is normally the case), the second trial values for ε in step 2, and ρ_2 in step 4 can be had by taking the values calculated for ε and ρ in steps 9 and 7 respectively, and using them as respective inputs for steps 3 and 5. Although subsequent trial values can established by repeating this procedure, this process can be greatly expedited by employing an iterative numerical solution technique such as the secant method for the third and all subsequent trial values.

3.2.3 Computer Program

To actually perform the steps described above, solve the oblique shock wave problem, and thereby generate the external flow data for each point on the trajectory, a microcomputer based program was developed using a QuickBasic compiler. However, before being applied to the external flow problem, the accuracy of the oblique shock wave solver portion of the program was successfully validated with the aid of sample calculations from Zucrow and Hoffman (1976).

For this investigation the computer program assumed a constant value of 1.4 for the specific heat ratio for ambient air at each trajectory point. This assumption was made for two reasons. First, although temperature variation for freestream conditions was large enough to produce changes in the specific heat ratio for air, these changes were small enough to be insignificant. Second, the Scramjet cycle code used to establish internal flow conditions (described below) for the supersonic nozzle illustrated in Figure 8, assumed a constant value of 1.4 for the freestream specific heat ratio for air. The need for consistency dictated that the method for solving the oblique shock wave problem be compatible with the calculation for internal flow conditions since both used freestream flow parameters as inputs. All other calculations involving temperature changes assumed temperature dependent specific heat ratios

39

based on data contained in NASA SP-273 (Gordon and McBride, 1971).

In addition to solving the oblique shock wave problem, the microcomputer program for external flow conditions also incorporated subroutines for the trajectory calculation, and the standard atmosphere equations. This effectively automated the external flow calculation process to the point where the only parameters that required specification prior to running the program were initial Mach number, Mach number increment, number of trajectory points, wedge (vehicle) half angle δ (see Figure 7), and initial guess for ϵ (for the perfect gas oblique shock wave solver). From this input, the program generated output for freestream as well as external flow conditions. Flow data for these two conditions for the various trajectory locations are presented in Table 1 and Table 2.

In using this program to generate data for freestream and external flow conditions, the 1962 US Standard Atmosphere model was employed for all atmospheric model calculations. Although data from the 1976 US Standard Atmosphere model was available, the decision was made for reasons of compatibility with the Scramjet cycle code (described below). It should be noted that for the range of altitudes examined in this study, these two models are virtually identical, thus there was no loss in accuracy.

For determination of altitude from Mach number and the standard atmosphere, geopotential altitude was first computed, then converted to geometric. All computations made by this program were performed using double precision variables.

3.3 Internal Flow

Before the effect of nozzle design or nozzle external flow on nozzle internal flow can be analyzed, these nozzle internal flow conditions must first be established. An enlarged view of this nozzle section is illustrated in Figure 8. Since, for the purposes of this study, internal flow is simply the result of the combustion of fuel and air in the combustion chamber of a supersonic combustion ramjet engine, it was therefore necessary to find a means of modeling the flow properties generated by a Scramjet engine. This was accomplished with the aid of a Scramjet cycle analysis code. Although originally developed for a mainframe computer (Craig, 1962) the version of this program used for this study was adapted from the original for use on a microcomputer (Smith, 1987).

This simulated engine operates on a very simple principle. The freestream air is diffused by the inlet to a supersonic velocity slightly lower than the original freestream. This diffusion is enough to raise the static temperature of the air above that required for autoignition,

41

thus no flame holders are required in the combustor. Fuel

is injected into the air at the entrance of the combustion

chamber where mixing and subsequently burning occur. The

combustion products are then exhausted from the combustion

chamber to the nozzle, producing a propulsive jet (Craig and

Ortwerth, 1962:1).

3.3.1 Cycle Code Assumptions

In using the Scramjet cycle code, several different

assumptions and approximations were made. These assumptions

and approximations effectively narrowed, to a more

manageable level, the scope of the problem of applying the

cycle code. Assumptions were also made not to avoid

complications, but because not enough specific information

was available to define the problem to be analyzed.

Assumptions made for these reasons include:

1. The conditions of the air entering the engine are the
    same as those corresponding to the undisturbed free
    stream and are determined by specifying flight Mach
    number and altitude.

2. Viscous and shock wave losses in the inlet were
    accounted for through the use of the inlet process
    efficiency parameter η_{KD}.

3. Nozzle and combustion losses were accounted for through
    the respective use of the nozzle velocity coefficient
    parameter C_V, and the combustion efficiency parameter
    η_c.

4. Except for the region where frozen flow may be defined
    in the nozzle, the flow is in equilibrium everywhere.

5. Temperatures remained low enough to prevent the
    occurrence of ionization in the flow.

6. The engine combustion chamber was long enough to allow for effective completion of the mixing and burning processes.

7. Combustion was for a stoichiometric fuel to air ratio composition.

8. Hydrogen was the only fuel used for this analysis.

3.3.2 Cycle Code Input Data

For the Scramjet cycle code to work properly and produce the output data needed to run the FDS program, 14 input parameters were required. A list of these input parameters is presented in Table 3. From the standpoint of program operation, these parameters can be divided into three categories: engine specific parameters, trajectory specific parameters, and variable parameters. The engine specific parameters were those that were the same for all of the different cases investigated at each trajectory point. These parameters included: fuel air ratio, combustion efficiency, fuel velocity ratio, fuel temperature, nozzle velocity coefficient, inlet entrance/nozzle exit area ratio, freezing point/combustor exit area ratio, flow type designator (equilibrium or frozen), and inlet efficiency type designator (η_{KD} or η_{KE}). The trajectory specific parameters were those that varied with each trajectory point chosen. These parameters were limited to altitude and freestream Mach number. The variable parameters encompassed the three remaining inputs. Included in this category were

43

inlet efficiency, diffusion ratio, and combustion process
type (constant area or constant pressure). These last three
parameters were the only ones used to adjust the program
output to meet the constraining requirements for engine
operation.

It should be noted that every effort was made to keep
this aspect of the calculation as simple as possible to
avoid unnecessarily complicating the process for determining
the internal nozzle flow conditions at each trajectory
point. Given the fact that some major assumptions and
simplifying generalizations have been made throughout the
course of this investigation, these assumptions pose no
threat to the accuracy or validity of the investigation.

3.3.3 Cycle Code Constraints

Although there was a certain amount of latitude as to
the variation of the input parameters for the cycle code,
some constraints did exist that served to narrow the scope
of the effort to establish internal nozzle flow conditions.
Generally, these limitations were based on physical
constraints that would be pertinent factors for a real
Scramjet combustor. These constraints included:

1. Static temperature at the inlet to the combustor had to
    be greater than or equal to 1800 degrees Rankine.
    Temperatures lower than this value would not allow for
    spontaneous or autoignition of the hydrogen fuel (Craig
    and Ortwerth, 1962:1).

2.   Static temperature at the combustor exit could not exceed 6000 degrees Kelvin. Remaining below this value mitigated the need to account for the ionization of the species generated from combustion. Thus, the computation was simplified. This limitation was "built-in" to the Scramjet program (Craig and Ortwerth, 1962:1).

3.   Static pressure at the inlet to the combustor had to be greater than 7.3 psi (about half an atmosphere). Pressures lower than this amount would not provide conditions favorable to reaction (Curran and Stull, 1963:8, Lefebvre, 1983:223).

4.   Static pressure at the inlet to the combustor had to be less than 50 psi (about 3.4 atmospheres). Pressures greater than this amount would produce stresses too large for the engine to withstand structurally. This parameter was adjusted by varying both the diffusion ratio and inlet efficiency.

5.   Mach number at the exit of the combustor had to be greater than 1. Subsonic flow conditions cannot be used as an input to the FDS code. Consequently, all combustor exit flow used in this study had to be supersonic. To meet this need for the Mach 7.5 case, a constant pressure combustion process was required. Diffusion ratio and inlet efficiency alone could not be adjusted to solve this problem for this case. In all other cases, combustion occurred as a constant area process.

6.   Capture area ratio (i.e., the ratio of cross sectional areas of inlet entrance and inlet exit, or A_0/A_2) had to be less than or equal to 50 (Curran and Stull, 1963:13).

7.   It was required that the combustion chamber cross section area exhibit smooth, continuous variation over the trajectory. Smooth area variation led to a relatively linear diffusion ratio schedule. This requirement came about from the need for monotonic geometry variation from a control and seal standpoint. It also served to further narrow the scope of the effort to define the parameters establishing internal flow.

45

3.3.4 Cycle Code Output

Although this program produced flow condition data for each station in the "simulated" engine developed in this portion of the study, only four parameters at each trajectory point were required from the cycle code. These data became the initial value line properties for the internal nozzle (Doty, 1991:55) for the FDS program, and included static pressure, static temperature, molecular weight, and Mach number at station 3, the exit to the combustor. Table 4 presents these data for each of the six points on the trajectory.

3.4 Thrust Analysis

Once the initial value line properties for both the internal and external nozzle flows (lines AO and HI in Figure 8) were established using the cycle code and the oblique shock wave solver, it was then possible to use the FDS code to begin the thrust analysis portion of the investigation. For this effort, all initial value line flows were assumed to be uniform. Except for a flat plate nozzle used for purposes of comparison, all nozzles were parabolic. This portion of the investigation consisted of repeated runs of the FDS code using different initial conditions and/or nozzle geometry. This of course reflected either the different flow conditions associated with each trajectory point, or the evaluation of the various nozzle or

cowl parameters. What follows is a brief description of the input data and calculation parameters that were varied in conducting this investigation.

3.4.1 Input and Output Files

For the FDS code to work properly, and the analysis to proceed, data describing the particular situation being modeled had to be specified. Computation commenced after these data were read by the program from a standardized input file. Data from this file fell into one of four different categories. These categories included: flow parameters (for internal and external initial value lines), geometry parameters (for nozzle and cowl specification), calculation parameters (for analysis and optimization computation), and output type specification parameters. It should be noted that not all of the data contained in the file required modification each time a different analysis was run. Enough commonality existed between the different trajectory points so that this was not required.

The output file that resulted from running the code on the input data for this application consisted of a copy of the input file, a listing of flow properties at each node along the initial value line (internal and external), and a table that summarized the thrust that had been produced. Although other formats were possible, this type proved most convenient for the present investigation. From these output

47

files, once it had been determined that no anomalous behavior was being exhibited, the thrust summary was extracted and placed in a spreadsheet file for further data reduction.

The thrust summary contained values for axial thrust from four different components. These components consisted of thrust produced due to the initial value line, OA in Figure 8, the upper nozzle wall (i.e., the surface described by ABC in Figure 8), the upper cowl (i.e., the surface described by ODEF in Figure 8), and the lower cowl (i.e., the surface described by HGF in Figure 8). The thrust summary also contained values for the summation of the wall thrust and total thrust, as well as statistical data relating the percentage that each component contributed to these totals.

3.5 Nozzle Design Procedures

For the purposes of this study, designing a nozzle for a hypersonic vehicle consisted of three operations. These operations were: optimization of the nozzle wall attachment angle, a parametric analysis to determine the effect of attachment angle on off-design performance, and a parametric analysis to determine the effect variation of cowl deflection had angle on thrust performance. What follows is a brief description of the procedures followed and methods used in performing these three operations.

48

3.5.1 Nozzle Wall Attachment Angle Optimization

This phase of the investigation consisted primarily of determining thrust performance for various nozzle attachment angles for the nozzle illustrated in Figure 8 at each point on the trajectory. During this phase, the cowl angle was maintained at zero degrees. From this information, the maximum thrust and the angle that produced this maximum thrust for each trajectory point was determined. This task was accomplished using an automated search procedure and is described below.

3.5.2 Direct Search (Doty, 1991:Sec 4.5)

The optimization procedure used for this portion of the study is a one parameter direct search method. A typical parabolic nozzle contour (not to scale) is shown in Figure 9, and is given by the following equation:

$$y^2 + c_1 x + c_2 y + c_3 = 0 \qquad (45)$$

The circular arc, line AB, has been expanded for clarity. The exit position of the nozzle, point C, is fixed and the circular arc radius of curvature, r, is specified. By fixing both the exit position of the nozzle and the circular arc radius of curvature, the only free parameter remaining to describe the parabolic nozzle contour is the circular arc attachment angle to the nozzle wall, θ_B. The parabolic

function describing the nozzle contour is developed in Doty, 1991: 224-231.

A manual search of nozzle wall thrust as a function of circular arc attachment angle produces the type of plot illustrated in Figure 10. The flat region where the slope, or derivative, of wall thrust with respect to attachment angle is zero provides the nozzle contour with maximum thrust. While a manual search may be effective in locating the nozzle contour for maximum thrust, an automatic direct search is typically more efficient and requires no user interface. The secant numerical method was chosen for the direct search optimization procedure.

A direct search is made using various attachment angles, and therefore different parabolic nozzle contours, to determine the nozzle contour which provides maximum thrust. Three guesses for the attachment angle are used to establish the basis for the secant method to numerically determine the slope of wall thrust as a function of circular arc attachment angle. As illustrated in Figure 10, an initial guess for the attachment angle is chosen arbitrarily. The flowfield for this initial attachment angle is analyzed and the thrust produced by the nozzle contour is calculated. Two succeeding guesses for the attachment angle are then obtained by perturbing the initial attachment angle a small amount, typically less than or

equal to one degree. The nozzle thrust for each of these
new attachment angles is also calculated. A summary of the
terminology used for the optimization is listed below:

Thrust 1 = thrust calculated for first attachment angle
Thrust 2 = thrust calculated for second attachment angle
Thrust 3 = thrust calculated for third attachment angle
  $(\theta_B)_1$ = first guess for attachment angle
  $(\theta_B)_2$ = second guess for attachment angle
  $(\theta_B)_3$ = third guess for attachment angle

Subsequent guesses for the attachment angle, θ_B, are
provided by the secant method. The derivative of thrust
with respect to attachment angle θ_B between iterations 1 and
2 is approximated as:

$$\left(\frac{d(Thrust)}{d(\theta_B)}\right)_{1,2} \approx \left(\frac{(Thrust\ 2) - (Thrust\ 1)}{(\theta_B)_2 - (\theta_B)_1}\right) \qquad (46)$$

Similarly, the derivative of thrust with respect to
attachment angle between iterations 2 and 3 is approximated
as:

$$\left(\frac{d(Thrust)}{d(\theta_B)}\right)_{2,3} \approx \left(\frac{(Thrust\ 3) - (Thrust\ 2)}{(\theta_B)_3 - (\theta_B)_2}\right) \qquad (47)$$

The slope used for the secant method is then:

$$slope = \left[\frac{(d(Thrust\ 2)/d(\theta_B))_{2,3} - (d(Thrust\ 1)/d(\theta_B))}{(\theta_B)_{2,3} - (\theta_B)_{1,2}}\right] \qquad (48)$$

51

where

$$(\theta_B)_{1,2} = \left(\frac{(\theta_B)_2 + (\theta_B)_1}{2} \right) \qquad (49)$$

$$(\theta_B)_{2,3} = \left(\frac{(\theta_B)_3 + (\theta_B)_2}{2} \right) \qquad (50)$$

The new attachment angle is then obtained by application of the secant method. Thus:

$$[\theta_B]_{new} = [(\theta_B)_3 + 2(\theta_B)_{2,3}] - 2 \left[\frac{(d(Thrust)/d(\theta_B))_{2,3}}{slope} \right] \qquad (51)$$

A new nozzle contour is constructed using the new attachment angle obtained from Eq (51). The optimization procedure is repeated until the thrust between iterations does not change more than a specified tolerance.

3.6 Nozzle Attachment Angle Off-Design Analysis

With the establishment of an optimum nozzle attachment angle for each trajectory point, an off-design performance analysis is then made. This analysis is conducted to determine which nozzle configuration suffers the least thrust reduction when operated at an off-design condition. To accomplish this analysis, a procedure is followed that involves starting with the nozzle attachment angle that

52

produces maximum thrust at the first point on the trajectory, and then determining thrust performance at all of the other points on the trajectory using only that particular configuration. The next step in this analysis is to take the attachment angle for the next point on the trajectory, and again determine thrust performance at all of the other points on the trajectory, using only the attachment angle for maximum thrust at the second trajectory point. The process is repeated in this manner until it is performed for all of the attachment angles on the trajectory. This off-design analysis amounts to a comparison of thrust produced by each of the optimum nozzle attachment angles, as they are analyzed at trajectory points other than those where they produce optimum thrust. From the data that result from this process, a selection is made of the one nozzle attachment angle that produces the smallest losses from off-design performance over the entire trajectory. The attachment angle identified from this analysis becomes known as the nozzle attachment angle for best off-design performance, and is then used exclusively in the third and final phase of this study.

3.7 Cowl Deflection Angle Off-Design Parametrics

Selecting a single nozzle attachment angle for use over the entire trajectory, in the manner described above, introduces certain problems. Although there will be one

trajectory point where optimum performance will be observed, and non-optimum performance losses at the other trajectory points will be minimal, there will still be performance losses experienced at a majority of the trajectory points. It is even possible that these thrust losses might be large enough to prevent the vehicle from overcoming its own drag.

In an effort to alleviate this potential problem, and at the same time improve thrust performance for all points on the trajectory, a cowl angle off-design parametric analysis is performed. This analysis consists of maintaining the nozzle attachment angle at the value determined as providing best off-design performance, and then accomplishing a thrust performance analysis for various cowl angles. Simply stated, this analysis consists of a manual search of total wall thrust as a function of cowl angle. Here, total wall thrust is defined as the algebraic sum of the axial thrust components resulting from the surfaces of the upper nozzle wall, the upper cowl, and the lower cowl (see Figure 8). This search is performed for each point on the trajectory, and is considered successful when the largest value for total wall thrust is found for a particular trajectory point. The cowl angle that causes this total wall thrust is then identified as the best angle for that trajectory point. The data resulting from this analysis provides a means of determining which cowl angle

34

setting produces the greatest total wall thrust performance improvement over and above the off-design performance identified for the nozzle attachment angle alone.

Once the cowl angles for best off-design total wall thrust improvement at each trajectory point are identified, it is then possible to perform an analysis to determine which one suffers the least total wall thrust reduction when operated at an off-design condition. This final trade-off study amounts to a comparison of total wall thrust production for each of the best off-design cowl angles, as they are analyzed at trajectory points other than those where they produce this best off-design total wall thrust. This last investigation completes this study.

3.8 Packing of the Computational Grid

One of the options that can be specified using the calculation parameters identified previously is the packing of the computational grid. Figure 11 illustrates the different packing schemes. As initially configured in the internal flow for the optimization of the nozzle, this parameter was set to so that the grid points would be concentrated more heavily toward the upper and lower portions of the channel, and less heavily in the center. This concentration was further biased toward the upper wall (i.e., toward the upper nozzle wall, and away from the cowl). Although this configuration tends to work reasonably

well for nozzle optimization, problems arise for cowl parametric studies. In the parametric portion of the investigation, this packing configuration produces numerical instabilities that made effective alysis impossible. For this reason, the packing had to be modified. The new configuration still concentrated grid points at the top and bottom of the channel and away from the center. However, this configuration involved no bias toward the top of the channel. Packing is weighted equally between the nozzle wall and the cowl region.
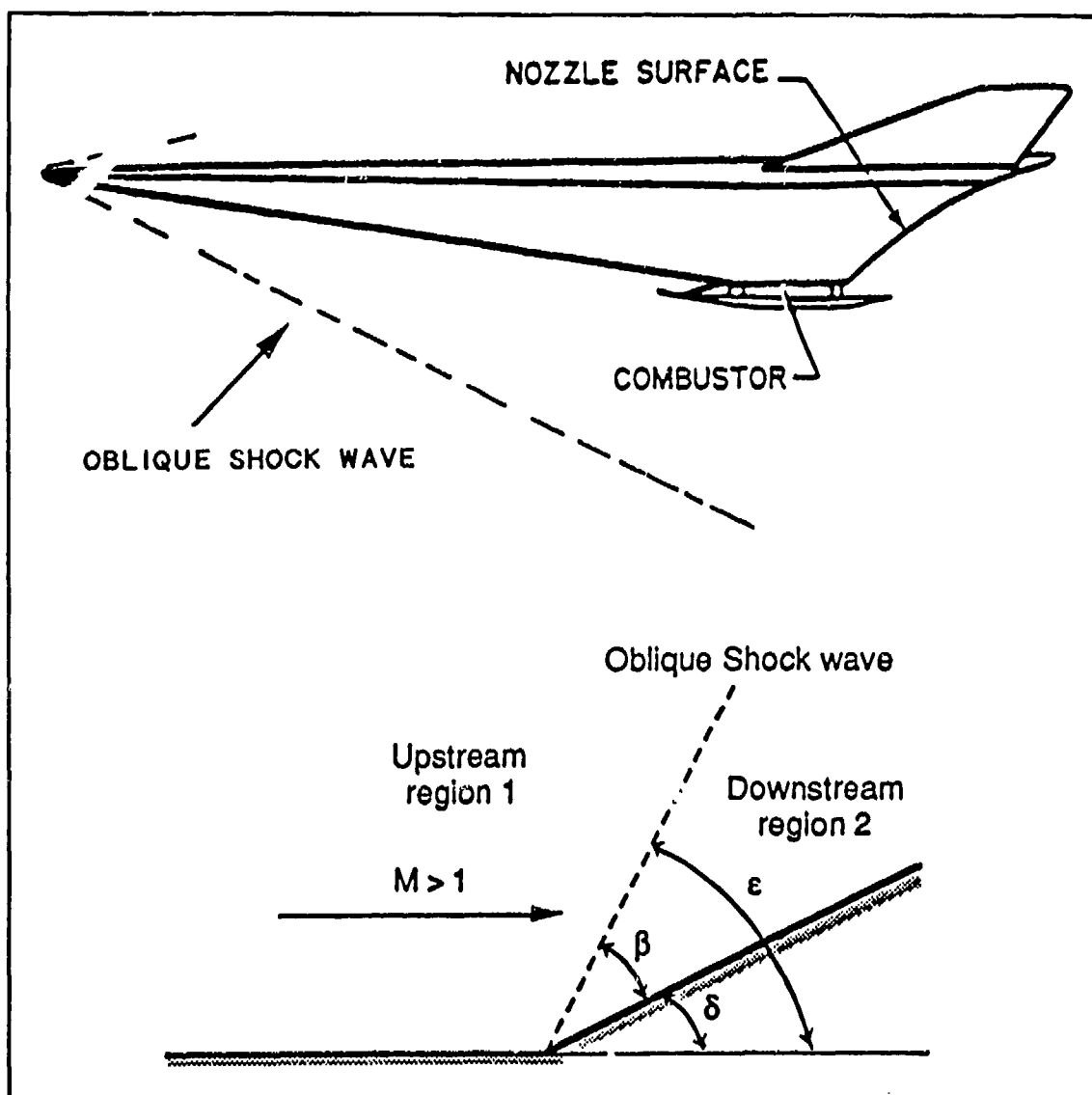
Figure 7. Oblique shock wave from vehicle interaction with freestream (Doty, 1991:180).
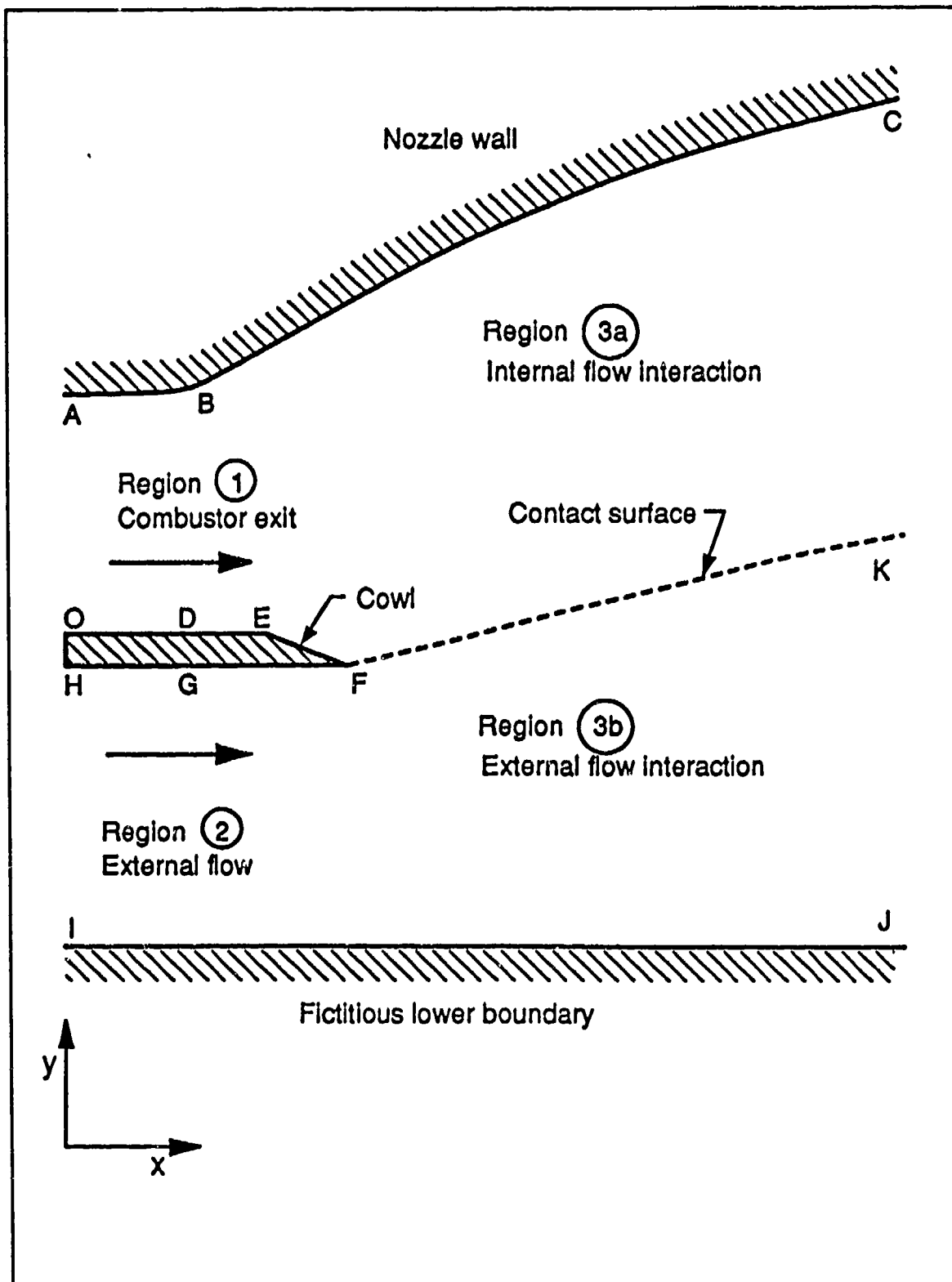
Figure 8. Internal and external nozzle flow and geometry. (Doty, 1991:68)

58
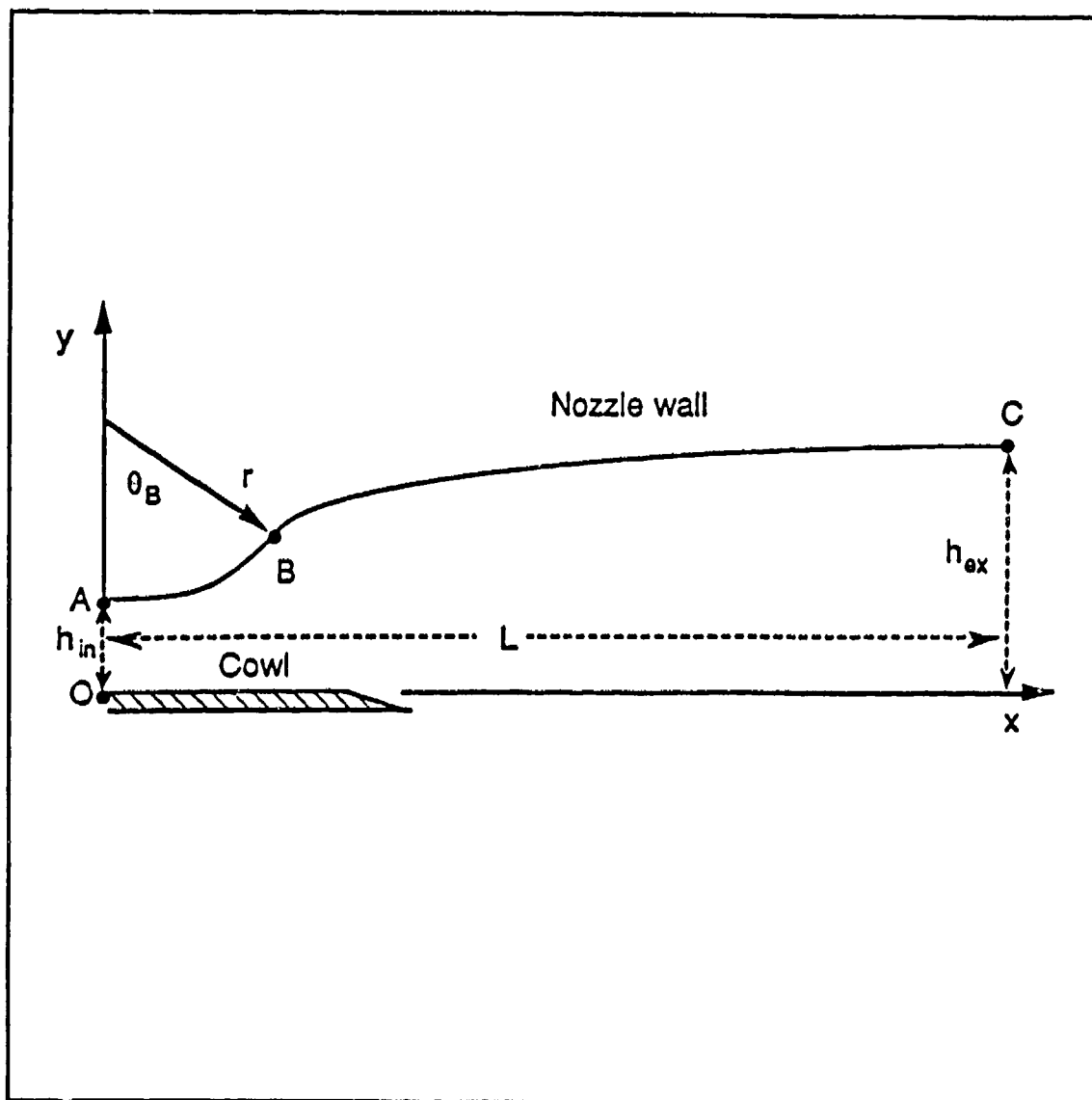
Figure 9. Circular arc and nozzle geometry (Doty, 1991:22).

59
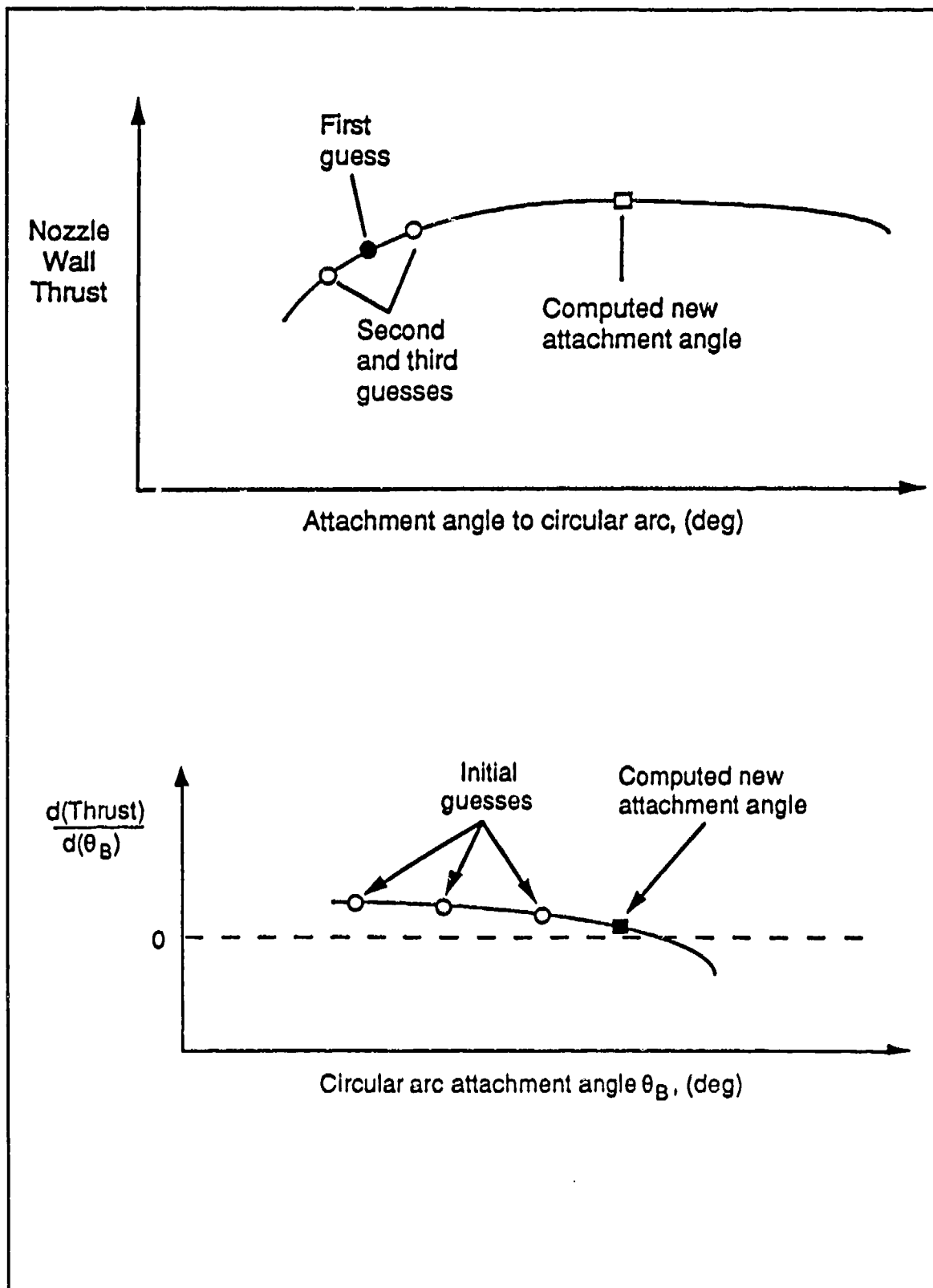
Figure 10. Optimization Procedure. (Doty, 1991: 65)

60
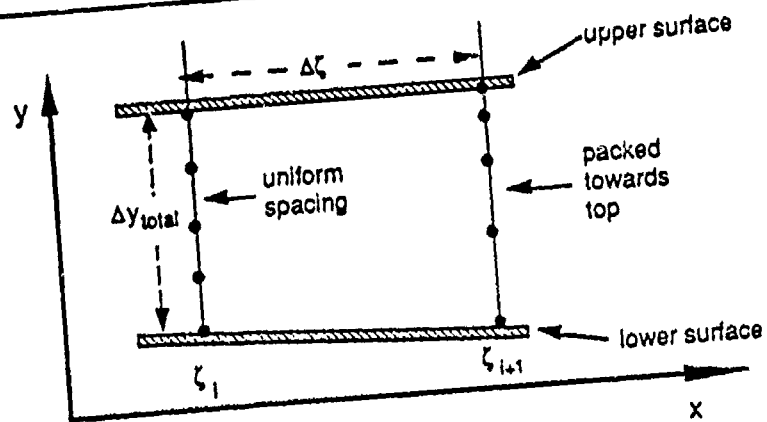
Packing grid points towards upper boundary.
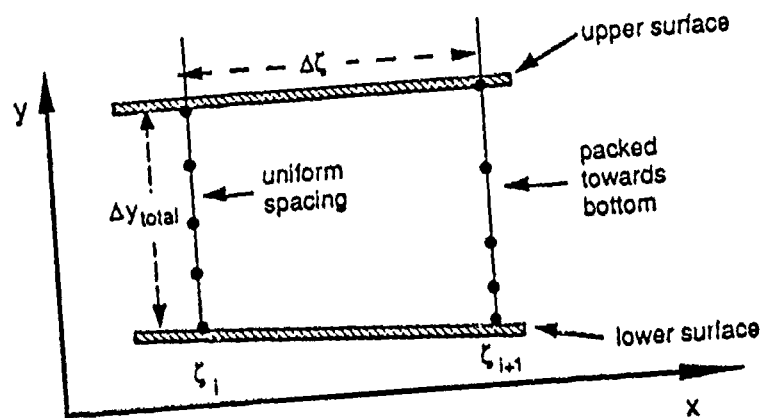
Packing grid points towards lower boundary.
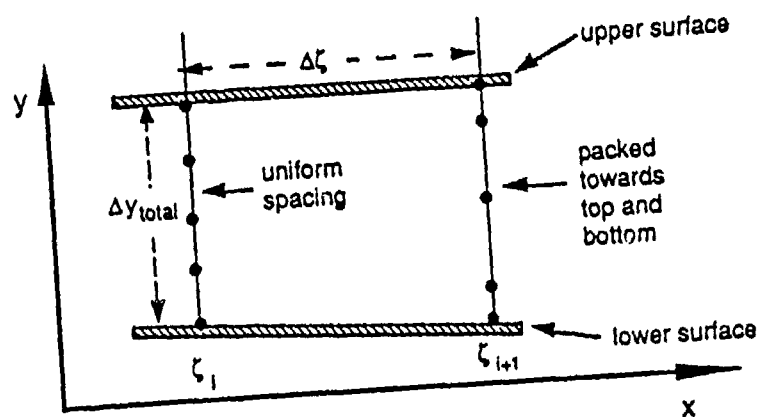
Packing grid points towards upper and lower boundaries.

Figure 11. Packing of the computational grid.
(Doty, 1991: 159-160)

Table 2. External flow conditions at each trajectory point.

External flow parameter	Value		
freestream Mach number	7.5	10.0	12.5
external flow Mach number	5.9	7.3	8.5
shock wave angle, ϵ (deg)	14.0	12.4	11.5
static pressure, P (N/m^2)	4452.79	3545.31	3095.61
static temperature, T ($^\circ$K)	348.7	420.5	512.2
density, ρ (kg/m^3)	0.044482	0.029372	0.021054
velocity magnitude, V (m/s)	2207.4	2998.9	3826.2
specific heat ratio, γ	1.398	1.394	1.385
gas constant, R_{air} (J/kg/$^\circ$K)	287	287	287

External flow parameter	Value		
freestream Mach number	15.0	17.5	20.0
external flow Mach number	9.4	10.3	11.0
shock wave angle, ϵ (deg)	10.9	10.6	10.3
static pressure, P (N/m^2)	2837.52	2673.86	2562.21
static temperature, T ($^\circ$K)	618.4	738.8	872.7
density, ρ (kg/m^3)	0.015984	0.012607	0.010228
velocity magnitude, V (m/s)	4666.8	5518.7	6380.5
specific heat ratio, γ	1.374	1.360	1.347
gas constant, R_{air} (J/kg/$^\circ$K)	287	287	287

Table 3. Cycle code input parameters.

INPUT PARAMETER
Altitude
Speed (Mach Number or Velocity)
Value of Inlet Efficiency
Type of Inlet Efficiency (KD or KE)
Diffusion Ratio V_2/V_0
Type of Combustion (Const. Pressure or Const. Area)
Type of Flow (Equilibrium or Frozen Flow)
Fuel Air Ratio (f/a)
Combustion Efficiency
Fuel Velocity Ratio (V_f/V_2)
Fuel Temperature for $V_f/V_2 > 0$
Full Nozzle Expansion, or Desired ratio for A_4/A_0
Freezing Point Area Ratio (A_{fp}/A_3)
Nozzle Velocity Coefficient (C_v)

Table 4. Internal flow conditions at each trajectory point.

Internal flow parameter	Value		
freestream Mach number	7.5	10.0	12.5
internal flow Mach number	1.74	1.96	2.77
static pressure, P (N/m²)	118031.4	471111.9	356714.1
static temperature, T (°K)	2554.3	2972.0	3033.9
density, ρ (kg/m³)	0.133833	0.448228	0.327945
velocity magnitude, V (m/s)	1757.5	2155.0	3084.0
specific heat ratio, γ	1.25	1.25	1.25
gas constant, R_{u} (J/kg/°K)	345.3	353.6	358.5

Internal flow parameter	Value		
freestream Mach number	15.0	17.5	20.0
internal flow Mach number	3.57	4.40	5.22
static pressure, P (N/m²)	264207.1	193018.7	142914.5
static temperature, T (°K)	3057.3	3046.7	3035.8
density, ρ (kg/m³)	0.238332	0.173506	0.127964
velocity magnitude, V (m/s)	4011.5	4947.7	5866.6
specific heat ratio, γ	1.25	1.25	1.25
gas constant, R_{u} (J/kg/°K)	362.6	365.1	367.9

64

IV   Results And Discussion

4.1   Introduction

The stated purpose of this investigation was to
evaluate parameters for an optimized thrust planar
supersonic nozzle over a typical hypersonic trajectory. As
part of an effort to determine the influence of
cowl/external flow on nozzle performance, an off-design
parametric analysis was to have been performed. This effort
was successful.

What follows is a discussion that presents the result
of this evaluation and subsequent parametric analysis.
Maximum thrust nozzles were designed for each point on the
trajectory using the FDS code and the optimization procedure
described in Section 3.5. From this information, a best
overall nozzle design was selected based on minimum off-
design performance losses. This best overall nozzle was
then employed, using procedures outlined in Section 3.7, to
perform off-design parametrics that demonstrated the effect
of cowl angle on nozzle performance for the best overall
nozzle.

4.2 Design of Best Nozzle

4.2.1 Determination of Optimum Nozzle Angle

The nozzle optimization portion of the study began with
application of the FDS code to the combined
internal/external flow nozzle discussed previously. The
geometry for this nozzle is illustrated in Figure 12.

The FDS code used as inputs for the internal and
external nozzle initial value properties, the respective
outputs from the Scramjet cycle code and the oblique shock
wave solver. Complete details of internal, external, and
freestream conditions for each Mach number on the trajectory
are presented in Table 1, Table 2, and Table 4,
respectively. An enlarged view of the cowl configuration is
shown in Figure 13. During this phase of the study, cowl
angle was maintained at zero degrees. Details of the nozzle
and cowl geometry parameters are presented in Table 5 and
Table 6, respectively.

The nozzle attachment angle that produced optimum
thrust was then determined for each one of the six points on
the flight trajectory using the direct optimization
procedure. A partial manual parametric study of nozzle wall
thrust as a function of attachment angle was also performed.
The data generated from this portion of the optimization
were used to provide more representative nozzle angle-thrust
trend information. This was needed primarily because the

direct optimization, although it quickly converged to a maximum, usually did not produce enough thrust data to clearly illustrate trend behavior. Trend information for each point on the trajectory is contained in Figure 14 - Figure 19. In general, the trends evidenced by these six plots seem to be parabolic in nature, and clearly show the nozzle attachment angles where extremum occur. Taking Figure 18 as a representative example, it is apparent that the maximum thrust occurs at 20.6 degrees.

Not readily apparent, and requiring some explanation, is the cause for this thrust behavior as attachment angle changes. With nozzle wall thrust defined as the thrust resulting from the axial contribution of pressure acting along the surface described by ABC in Figure 12, changes in pressure and/or area are the only things that can change the magnitude of this force. Since points A and C in Figure 12 are fixed, the axial projection of nozzle wall area (i.e., projection onto the y axis) is also fixed. So even though the nozzle configuration or shape and surface area can change, its projected area remains constant. Thus, only pressure changes in the nozzle can affect wall thrust.

These pressure changes in the nozzle are governed by the flow turning angle, since it determines whether the flow is expanded or compressed. Since nozzle wall geometry and thus flow angle are determined by nozzle attachment angle,

it becomes clear why varying the attachment angle can change the thrust. The trend illustrated in Figure 18 results because changing the attachment angle varies the flow angle. This in turn has the effect of varying the nature of the complicated interaction between shock waves and expansion waves that occurs within the nozzle. As the flow exits the combustor in Figure 12, it initially expands due to the oblique turning angle at point B. Waves from this expansion that could possibly interact with the contact surface illustrated in the figure, are also generated at this point. These waves could even reflect off of cowl surface ODEF onto the nozzle wall. Expansion waves that behave in a similar manner, can also result from the turning angle on the cowl at point E as well. As the flow travels along the nozzle wall, compression waves are generated due to the change in flow direction caused by the parabolic shape of the nozzle. These compression waves may or may not interact with the expansion waves or the contact surface. What is certain, is that pressure will change at various locations in the nozzle. And, as mentioned earlier, it is the pressure change that is responsible for the variation in thrust observed when in attachment angle is changed, as illustrated in Figure 18.

An extreme example of the variation that can result from this complicated interaction is illustrated in

Figure 19. Although certainly not a representative case, special note should be made of the trend in Figure 19, the plot for the case of flight at Mach 20.0. Here, this search procedure resulted in an optimum, a local maximum, and a local minimum. Though this behavior seems anomalous, it has been confirmed by Doty, et al. (1989), and has yet to be satisfactorily explained. However, it seems quite clear that an extremely complex interaction between compression waves, expansion waves, and contact surface is occurring.

Despite the trend behavior for the trajectory point at Mach 20, the values for maximum wall thrust from this and all of the other trend plots produced from this procedure were selected as the optimum for the corresponding trajectory point. This information is contained in Table 7, along with the corresponding nozzle attachment angles that caused these maxima. As the vehicle travels along its trajectory the general trend in nozzle attachment angle for maximum thrust as Mach number increases, is one of a monotonically decreasing function (except for the case of the trajectory point at Mach 7.5 where a constant pressure combustion process was used to simulate internal flow data). Also evident from the data presented in Table 7 is the fact that nozzle wall thrust varies significantly over the trajectory with an apparent trend that is similar to that of the nozzle attachment angle. Both parameters show trends

that are monotonically decreasing from the second trajectory point to the last one.

4.3   Selection of Nozzle Angle for Best Off-Design Performance

With the optimum nozzle for each Mach number determined, it was then necessary to decide which design performed best at all of the other Mach numbers (i.e., suffered the least reduction or "penalty" in thrust performance when operating at conditions other than those for which it was designed).

The rationale motivating this determination is quite straight forward. It was shown in the previous section that for each trajectory point, a different nozzle attachment angle was required to produce maximum thrust. A variable geometry nozzle would be required for a single vehicle to have a nozzle with a different attachment angle for each trajectory point. Such a device, along with its supporting systems, would add a significant amount of weight to the vehicle. As weight increases, so do performance losses. These losses may far exceed any gains in thrust brought about by nozzle optimization. For this reason, it may be more important to determine the nozzle design that produces the lowest losses in off-design performance over the entire range of Mach numbers in the trajectory. This is done by conducting an off-design thrust performance analysis.

This off-design analysis was accomplished by performing
the procedure outlined in Section 3.6, using the nozzle
attachment angles arising from the direct search. The
results from this procedure were then compared by plotting
on a single graph, as in Figure 20, the amount of nozzle
wall thrust produced by each nozzle design as a function of
flight Mach number. Seen here is a general trend followed
by all of the attachment angles, where the amount of thrust
produced starts out relatively small at Mach 7.5, increases
dramatically at Mach 10.0, then monotonically decreases in
an almost linear fashion, as flight Mach number approaches
20.0. Although the general thrust variation with Mach
number is primarily due to the ambient conditions extant at
each trajectory point, the rather low amount produced at
Mach 7.5, and the subsequent dramatic increase at Mach 10.0
is probably attributable to the fact that a constant
pressure combustion process was used to simulate internal
flow conditions for the Mach 7.5 trajectory point. Internal
flow for all of the other points on the trajectory were
simulated using a constant area combustion process (see
Section 3.3.3, Constraint 5). The data used in this
comparison are presented in Table 8. This table presents
the actual wall thrusts calculated (in Newtons per meter)
for the off-design analysis at each point on the trajectory.
The entries in Table 8 of "NA" indicate off-design analysis

71

points where the nozzle angle was too large for the FDS code

and the corresponding initial value line conditions to

converge to a solution. Thus thrust data were not available

for these trajectory points.

Upon examination of the data presented in Figure 20, it

is apparent that although a determination can be made for

Mach numbers 10.0 and 12.5, it would be extremely difficult

to determine which nozzle attachment angle performs best

over the entire trajectory for the other Mach numbers. This

occurs for the simple reason that there is very little

separation between the data points at the other Mach

numbers. Since the range of values for maximum thrust

determined in the optimization port.on of the study extend

from 3866 N/m to 18717 N/m, the resulting scaling factor

used to place all the data on a single graph precludes

significant separation in the data points at Mach numbers

7.5, 15.0, 17.5, and 20.0. Thus, comparison cannot proceed

unless a better plotting scheme is employed.

To more easily facilitate this comparison, normalized

nozzle wall thrust (i.e., a non-dimensional thrust or thrust

fraction) was also plotted for each Mach number as a

function of nozzle attachment angle in addition to actual

wall thrust as a function of Mach number. Values for

normalized nozzle wall thrust were established by dividing

the values of nozzle wall thrust at a particular Mach number

72

by the maximum thrust at that particular Mach number as
indicated in the following equation:

$$(normalized \; thrust_i)_{M1} = \frac{(thrust_i)_{M1}}{(optimum \; thrust)_{M1}} \qquad (52)$$

Here M1 is the freestream Mach number that identifies the
trajectory point, $(thrust_i)_{M1}$ is the "i th" thrust being
normalized at that trajectory point, and $(optimum \; thrust)_{M1}$
is the maximum thrust produced at that trajectory point.
This type of scaling allowed all of the values to be plotted
on the same graph in a meaningful fashion (the curve for the
nozzle attachment angle corresponding to maximum thrust at
Mach 7.5 is not included on the plot, since it failed to
produce solutions for the upper half of the trajectory, and
because the plotting routine used could only handle 6 curves
per plot). Before the normalization procedure, maximum
thrust values ranged from 3866 N/m to 18717 N/m.
Afterwards, all values for maximum normalized thrust were
equal to 1. The results of this procedure are presented in
Figure 21. Data used to plot this graph are contained in
Table 9. A thrust analysis of a straight nozzle with
attachment angle 13.511 degrees was also performed for each
Mach number on the trajectory, and is included in the figure
to provide a basis for comparison. The thrust for the
straight nozzle was normalized in the same manner as that of

73

the parabolic nozzle. Since all of the values for the linear nozzle were consistently lower than those for the parabolic nozzle, there was no normalized thrust for the linear nozzle equal to 1 (i.e., linear nozzle did not produce a maximum for any of the trajectory points).

Scrutiny of Figure 21 indicates evidence of several trends. Most obvious of these is that nozzle wall thrust fraction seems to generally increase over the course of the trajectory from Mach 7.5 to 20.0 after first decreasing slightly at the second trajectory point. Another trend illustrated in Figure 21 is that there seems to be considerable variation in wall thrust fraction over the trajectory range. Most significant is the fact that wall thrust fraction is seen to be more sensitive to changes in nozzle attachment angle at the lower Mach numbers than at the higher ones. This could be only an apparent trend due to the fact that curves for two of the attachment angles did not produce solutions at the high end of the Mach number range. However, the fact that the curves tend to be flatter and less dispersed at the upper ranges should not be dismissed, since the curves that possess these characteristics and also give good performance at the higher Mach numbers, are the ones most desirable for off-design performance. The curves for attachment angles of 20.6 degrees and 17.814 degrees specifically fall in this

74

category. Of these two, the curve for nozzle attachment angle of 20.6 degrees not only showed the flatter response to Mach number variation, but it also showed performance that was almost identical to that of the attachment angle that was optimized for flight at Mach 20.

From the information presented in Figure 21, it was determined that a nozzle attachment angle of 20.6 degrees (corresponding to optimum performance at Mach 17.5) provided the best off-design thrust performance over the Mach number range in the trajectory. Although this particular design suffered moderate thrust penalty at the lower Mach numbers, this decision was made primarily because there was only slight off-design performance degradation at the higher end of the Mach number spectrum. Since hypersonic vehicles are very sensitive to losses at the higher Mach numbers, and because even small losses can mean loss of engine thrust, or even loss of the vehicle, this decision was biased toward maximized performance at the higher speeds. Once this best overall nozzle design was determined, all subsequent analyses were performed using this nozzle design.

4.4 Design of Best Cowl

4.4.1 Cowl Angle Off-Design Parametric Analysis

The cowl parametric analysis portion of the study began with application of the FDS code to the combined

internal/external flow nozzle, and proceeded in a manner
similar to that of the nozzle optimization discussed
previously. During this phase of the study, nozzle
attachment angle was maintained at 20.6 degrees. Here, the
cowl angle was the only parameter that was varied. As
before, the FDS code used as inputs for the internal and
external initial value properties, the respective outputs
from the Scramjet cycle code and the oblique shock wave
solver. The enlarged view of the geometry for the variable
cowl used in this portion of the optimization is illustrated
in Figure 13. Details of the cowl geometry parameters are
presented in Table 6. A manual parametric analysis of total
wall thrust as a function of cowl angle was then performed.
The cowl angle that produced maximum thrust for this fixed
nozzle angle was subsequently determined for each one of the
six points on the flight trajectory from this analysis. The
data generated from this portion of the optimization were
used to provide cowl angle-thrust trend information in a
manner similar to that of the nozzle optimization. Thrust
versus cowl angle trend information for each point on the
trajectory is contained in Figure 22 - Figure 27. The
trends illustrated by these plots are very similar to those
produced for the nozzle optimization study. Both studies
exhibited trend behavior that was fairly parabolic in
nature. However, examination of the plots produced for the

cowl study shows trend curves that are rougher and more irregular than those for the nozzle study. Also for the cowl study, as Mach number increased, this behavior seemed to get worse. As far as roughness is concerned, this phenomenon is probably due to the fact that the numerical grid packing factor was adjusted to concentrate grid points more evenly at the upper and lower boundaries of the nozzle (see section 3.8). Although this eliminated the instabilities that prevented convergence to a solution, it had the added effect of somewhat reducing the accuracy of the solution calculated. The trend of this roughness becoming more pronounced as Mach number increased, is probably an example of the same phenomenon that produced an optimum, a local maximum, and a local minimum in the nozzle optimization study. Here however, because of the irregular nature of the thrust curves, it is difficult to identify the location of the local minima and maxima. In any event, the selection of best cowl deflection angle at each trajectory point is based solely on the cowl angle that produced maximum total wall thrust at each Mach number.

The fact that changes in cowl deflection angle could actually increase total wall thrust is again easily explained. With total wall thrust defined as the thrust resulting from the contribution of the pressure acting on the nozzle wall and the upper and lower cowl surfaces,

increases in pressure and/or area are the only things that can increase this thrust. By deflecting the cowl, both of these two parameters are affected.

As can be seen in Figure 12, when the cowl deflection angle is set to zero the only cowl area contribution is very small, and results from the upper cowl projection of surface EF onto the y axis. As a result of the pressure (which results from the complicated interaction between compression and expansion waves, described previously) in this region, the majority of the thrust comes from the nozzle wall surface ABC, with a small but positive contribution from the cowl surface. When the cowl is deflected in the positive direction for example (see Figure 13), this changes. Now the lower cowl area contribution is no longer zero. The area contribution is from upper cowl surface EF and lower cowl surface FG as well (here it is assumed that the deflection is less than 10 degrees). Since this deflection causes the complicated interaction between expansion and compression waves (described in section 4.2.1) which results in lower pressure in the external flow region, the thrust contribution from surface FG is a negative one (i.e., a drag force). Fortunately, the effect of this type of cowl deflection on the internal flow region serves to increase the pressure over the much larger surface area of the nozzle

wall. Thus the overall effect of this type of deflection is to increase the total wall thrust.

For deflection in the negative direction, expansion wave interactions serve to reduce the pressure in the internal flow region while compression waves serve to raise it in the external flow region. So for this case, even though the upper cowl pressure and area contribution increases, total wall thrust decreases since the pressure on these upper surfaces is lower than it was before the deflection. It was this type of pressure-area deflection angle behavior that produced the thrust trends illustrated in Figure 22 - Figure 27.

The cowl parametric analysis produced a value for maximum total wall thrust for each Mach number studied, and the corresponding cowl angle that caused this maximum. This information is contained in Table 10. When this information is plotted in a graph of cowl angle for maximum total wall thrust as a function of Mach number, what results is a schedule of cowl angles that would produce best performance for the fixed nozzle angle, over the course of the trajectory. This information is presented in Figure 28. When the thrust data from Table 10 is compared with the total wall thrust produced from a nozzle configuration with attachment angle 20.6 degrees but zero cowl angle (see Table 11), it is clear that this cowl angle schedule has

significantly reduced nozzle off-design performance losses.

4.4.2 Selection of Best Cowl Angle

Once the cowl angle for minimum losses at each Mach number was determined, it was then necessary to decide which cowl angle performed best at all of the other Mach numbers. Or stated another way, it was necessary to decide which cowl angle suffered the least penalty in thrust performance when operated at conditions other than those for which it was designed. This was accomplished through an off-design parametric analysis for the cowl angle.

This off-design analysis was accomplished by plotting on a single graph the amount of total wall thrust produced by each cowl design as a function of Mach number, and then comparing the results. Figure 29 illustrates the outcome of this procedure. The data used to plot this graph are contained in Table 12. Although this seems to be a single curve, what is actually being presented is a set of six curves that are so close in value that the scaling used makes them indistinguishable It is readily apparent that this type of operation will not produce a plot that will be useful in making this type of comparison. Thus, as was the case for the nozzle attachment angle off-design analysis, here normalized total wall thrust must be plotted instead of actual total wall thrust to more easily facilitate the necessary comparisons. As before, values for normalized

total wall thrust were established by dividing the values of total wall thrust at a particular Mach number by the maximum total wall thrust at that particular Mach number using Eq (52). Here, as with the off-design analysis described in Section 4.3, values for maximum normalized thrust were equal to 1. This type of scaling allowed all of the values to be plotted on the same graph in a meaningful fashion. These normalized data were then plotted in two different ways. The data used to create these plots are contained in Table 13.

First, to get an idea of thrust performance behavior as the cowl angle varied, normalized thrust, in curves of constant Mach number, was plotted as a function of cowl angle. The result of this procedure is illustrated in Figure 31. Examination of the information presented in this figure clearly shows that performance at the Mach 20.0 trajectory point is the one most sensitive to cowl angle variation. All of the other curves, over the entire range of cowl angles, appear to be relatively flat and fairly well clustered in the upper portion of the graph. This would indicate that these other cowl designs would exhibit only moderate reductions in performance when operated at off design conditions. Also significant is the fact that even small changes in angle setting at values very close to 4.3 (i.e., angle for best performance at Mach 20.0) produce

81

relatively large changes in total wall thrust fraction. This is evidenced by the fact that the slope of the line connecting the point at 4.2 degrees to the one at 4.3 degrees is very steep. In fact, it is much steeper than any point on the rest of the curve. The case of flight at Mach 20.0 is the only one this sensitive to cowl angle variation close to its maximum. These two trends indicate that for best performance, cowl angle selection should be biased toward flight at Mach 20.0.

Second, to understand how nozzle thrust performance varied for a nozzle with a fixed cowl over the trajectory, these data were plotted as a function of Mach number, in curves of constant cowl angle. The results of this analysis procedure are contained in Figure 30. The data used for these plots are presented in Table 13. Upon examination of this figure, three things become clear. First, the curve for the 4.3 degree displays the least variation over the entire Mach number range (i.e., the flattest curve). Since this is the deflection angle for best thrust at Mach 20.0, this is seen as another reason to bias the selection of best cowl angle toward the Mach 20.0 case. Second, thrust fraction for the Mach 10.0 and 15.0 cases, are very closely grouped. This means that very little variation in thrust performance is demonstrated over the cowl angle range from 2.2 to 4.3 degrees. Thus these two Mach numbers are very

insensitive to cowl angle variation, and need not be considered when selecting a cowl angle. And finally, except for the two highest Mach numbers, thrust performance in general displays very little variation over the Mach number range. However, it is also evident from this plot that the variation at the higher Mach numbers that does occur is more than twice as large as the variation at the other Mach numbers. This would indicate that performance losses could be minimized if the cowl were optimized for the Mach 20.0 case. For these reasons, it was determined that a cowl angle of 4.3 degrees (corresponding to optimum performance at Mach 20.0) provided the minimum performance losses over the entire Mach number range in the trajectory.

When contrasted with the performance attained when a variable cowl is used, the advantages of a constant cowl deflection angle are readily apparent. Figure 32 depicts thrust performance over the typical trajectory for the three cases of no cowl deflection, scheduled cowl deflection (variable cowl), and a constant cowl deflection angle of 4.3 degrees. This figure clearly shows that significant performance improvement is achieved over most of the flight trajectory with a constant cowl deflection angle of 4.3 degrees as compared to a zero cowl deflection angle. But more importantly, this figure shows that the improvement achieved is extremely close to the best improvement that

83

could be gained by using a variable geometry cowl. This

essentially means that it is possible to realize the

performance benefits of a variable geometry cowl without

having to pay the penalty of excess weight and added

complexity.
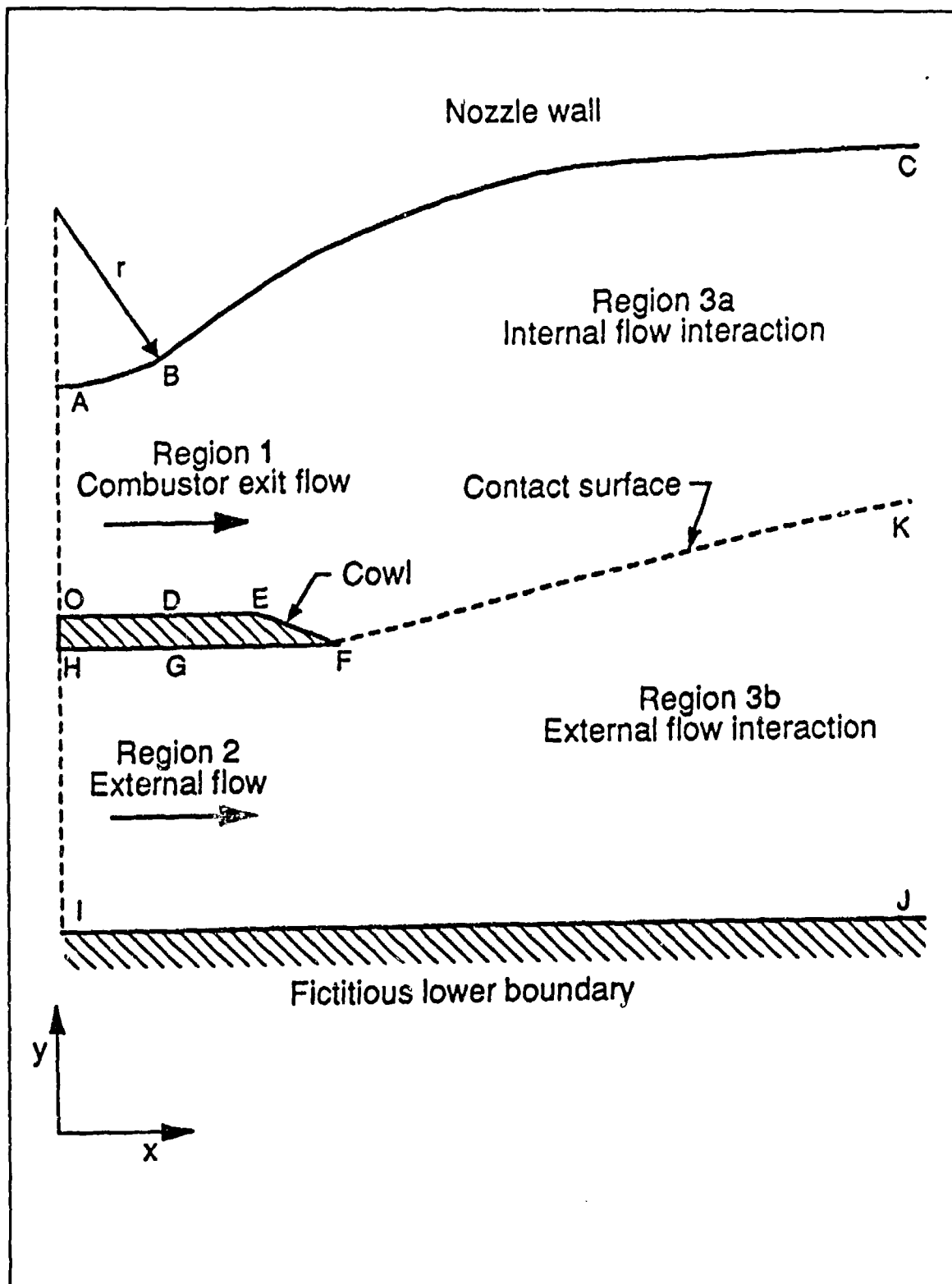
Figure 12. Internal and external nozzle flow and geometry.
(Doty, 1991: 68)

Figure 13. Examples of possible cowl configurations. (Doty, 1991, 69)

86
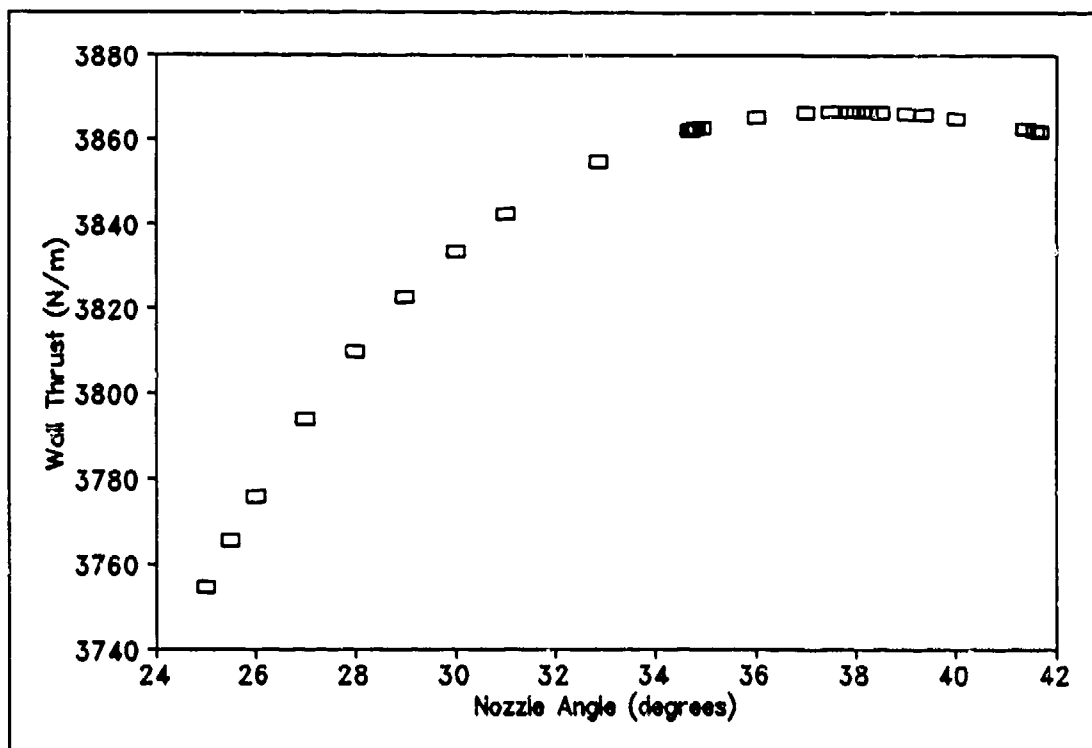
Figure 14. The effect of nozzle attachment angle on wall thrust for Mach number 7.5.
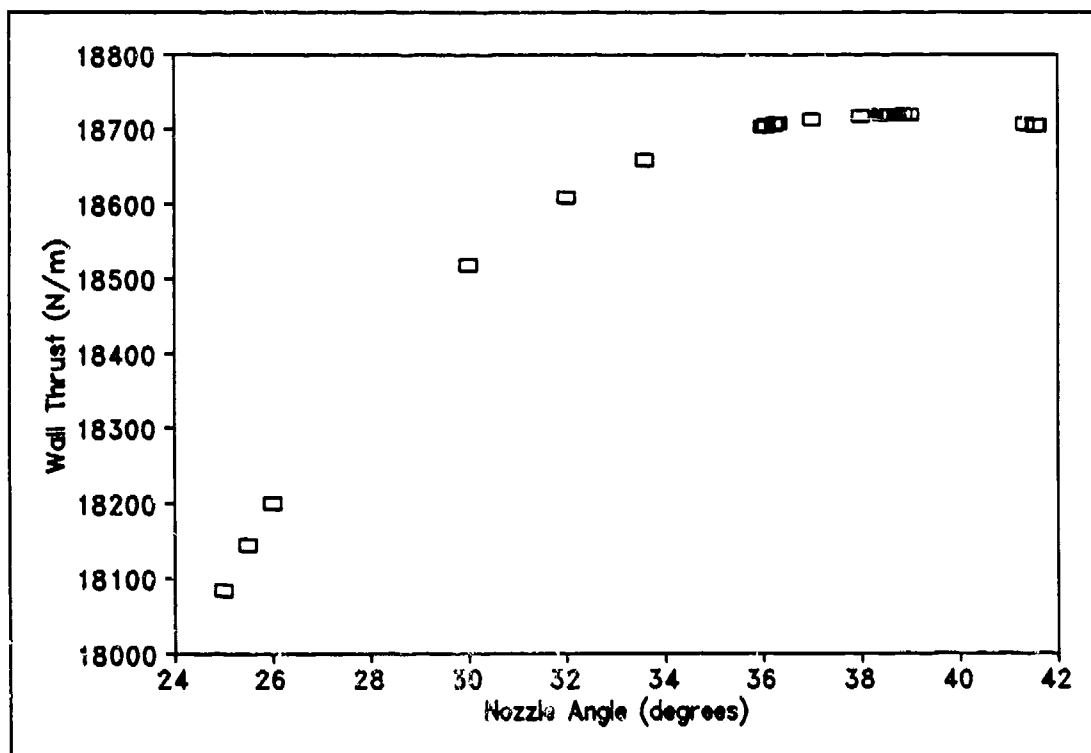
Figure 15. The effect of nozzle attachment angle on wall thrust for Mach number 10.0.

Figure 16. The effect of nozzle attachment angle on wall
thrust for Mach number 12.5.

Figure 17. The effect of nozzle attachment angle on wall thrust for Mach number 15.0.
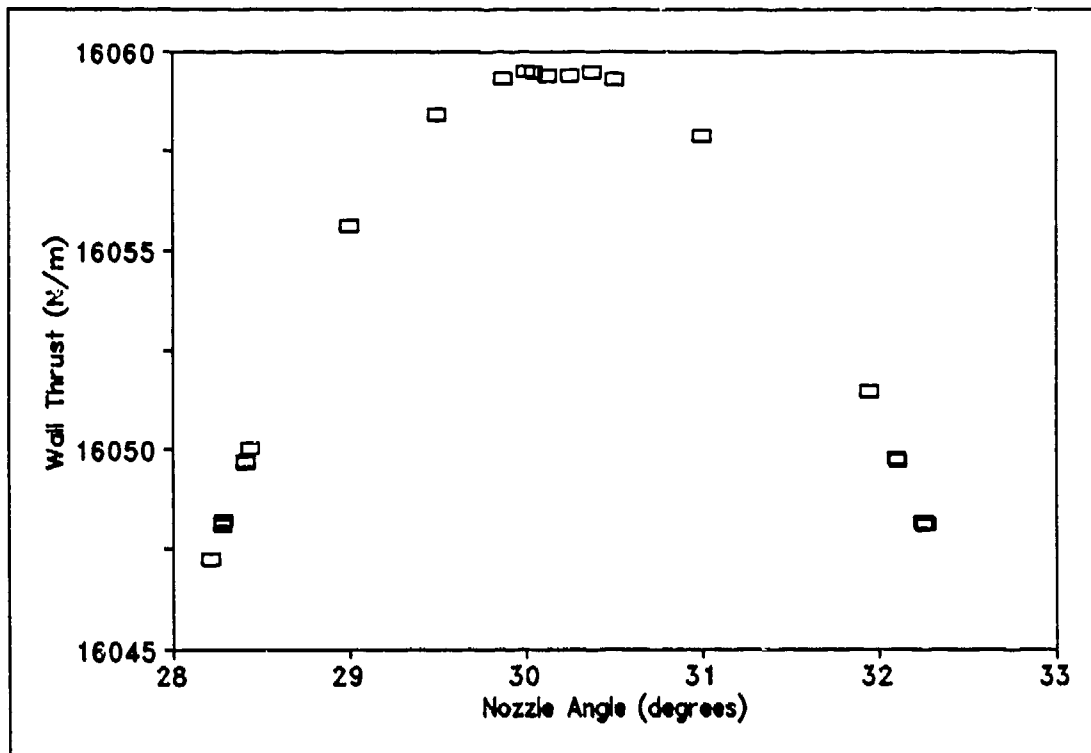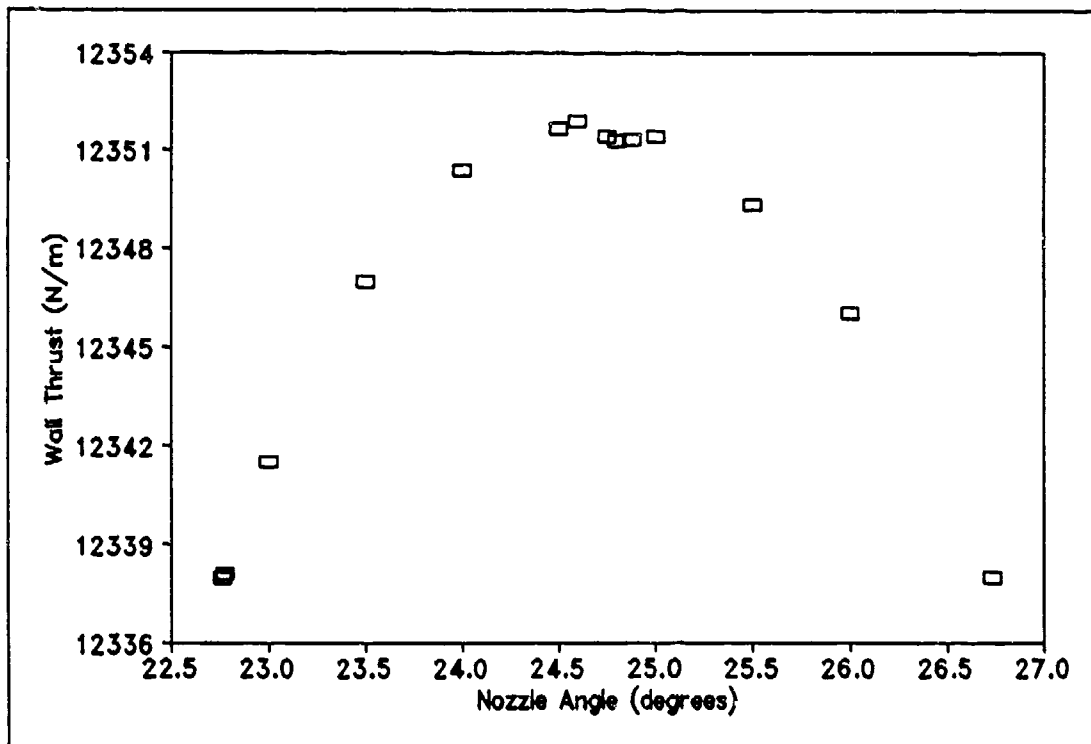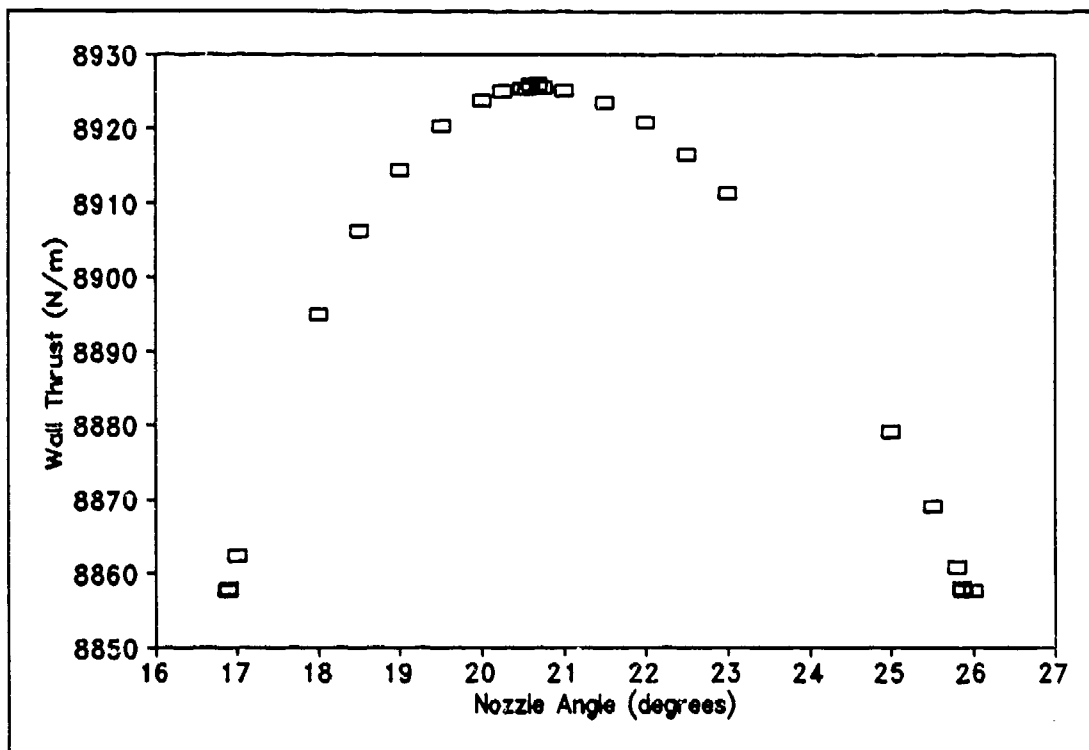
Figure 18. The effect of nozzle attachment angle on wall thrust for Mach number 17.5.
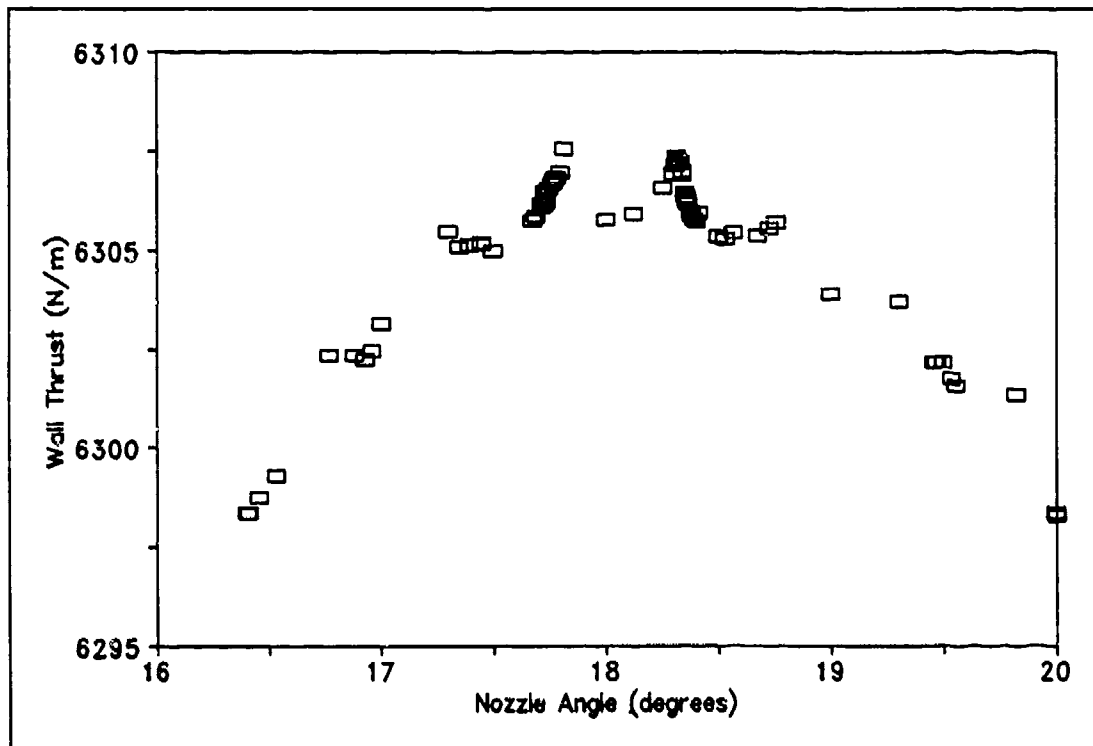
Figure 19. The effect of nozzle attachment angle on wall thrust for Mach number 20.0.
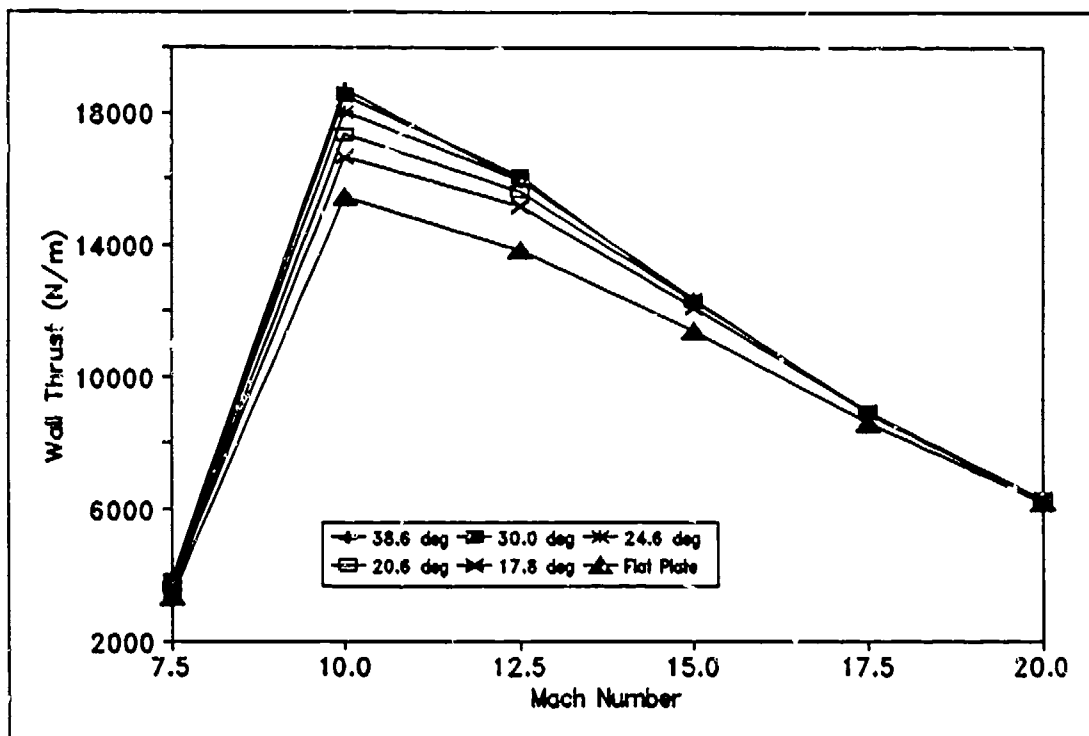
Figure 20. The effect of Mach number on wall thrust for various nozzle attachment angles.
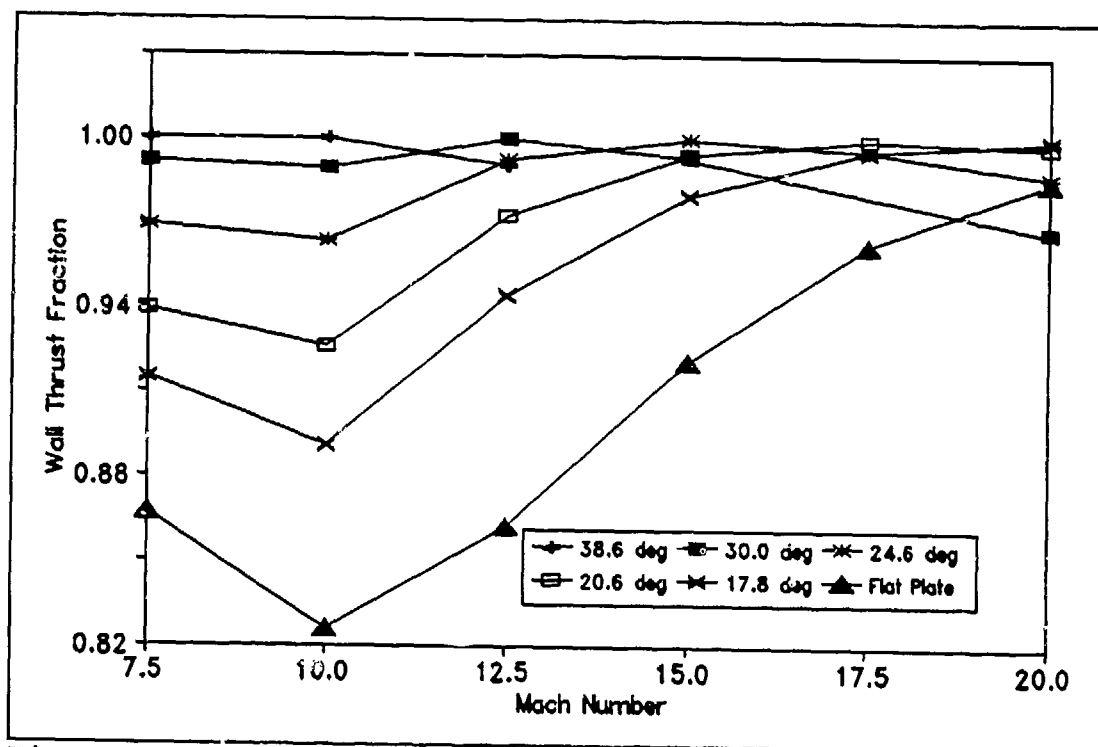
Figure 21. The effect of Mach number on wall thrust fraction for various nozzle attachment angles.
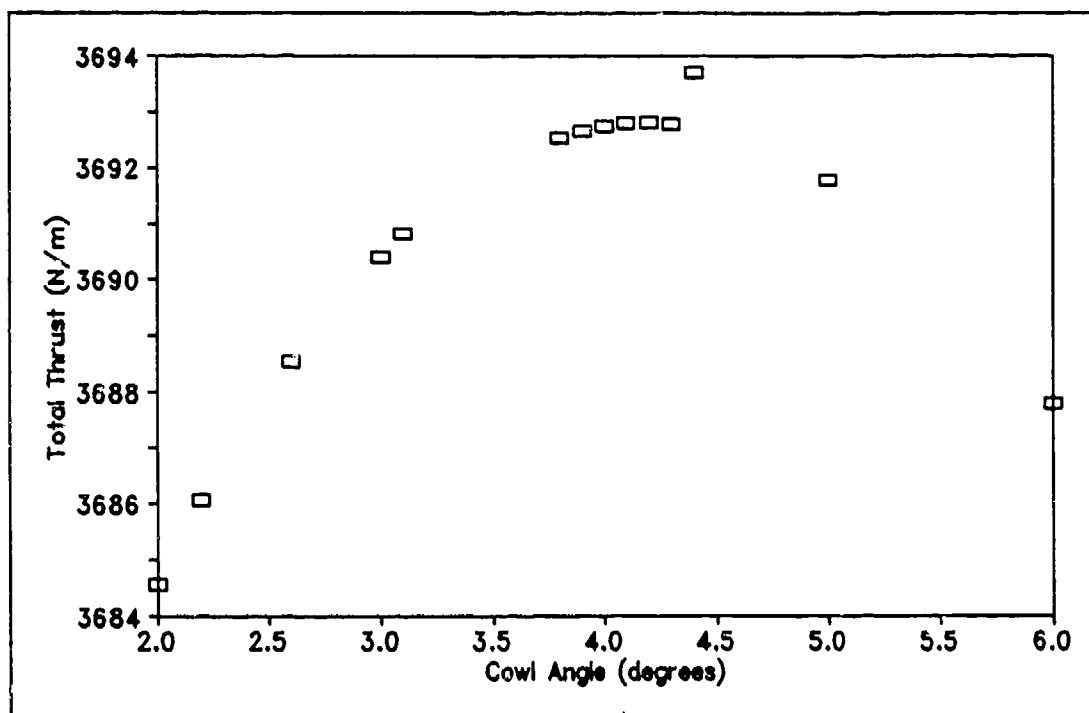
Figure 22. The effect of cowl deflection angle on total wall thrust for Mach number 7.5 and nozzle attachment angle 20.6 degrees.
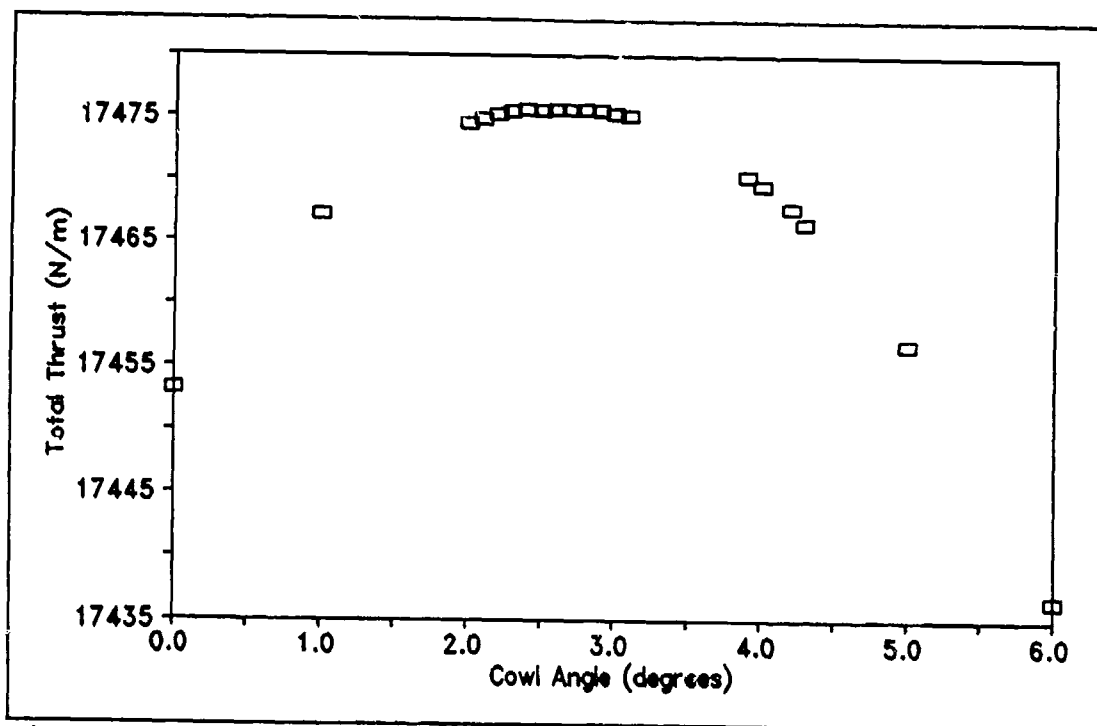
Figure 23. The effect of cowl deflection angle on total wall thrust for Mach number 10.0 and nozzle attachment angle 20.6 degrees.
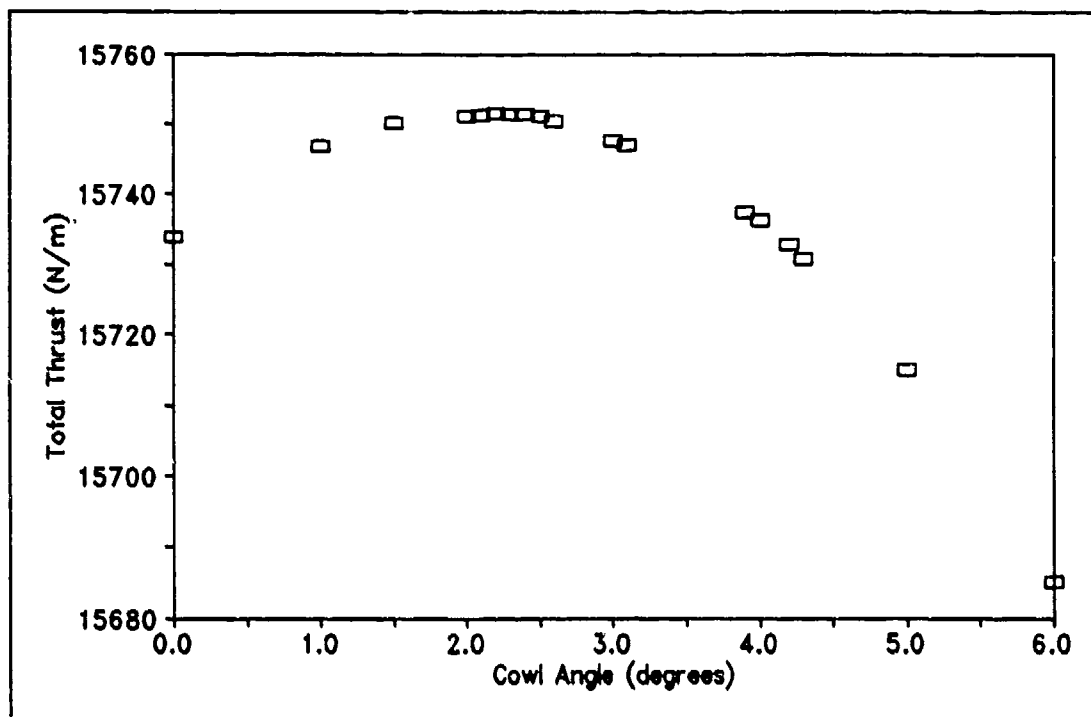
Figure 24. The effect of cowl deflection angle on total wall thrust for Mach number 12.5 and nozzle attachment angle 20.6 degrees.
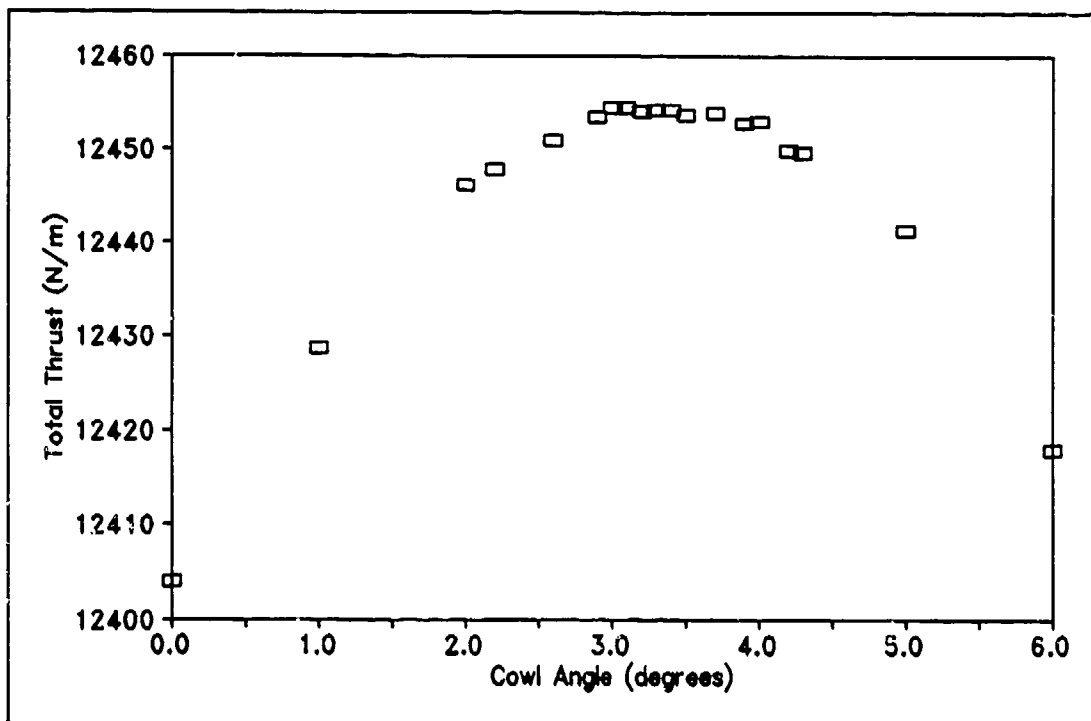
Figure 25. The effect of cowl deflection angle on total wall thrust for Mach number 15.0 and nozzle attachment angle 20.6 degrees.
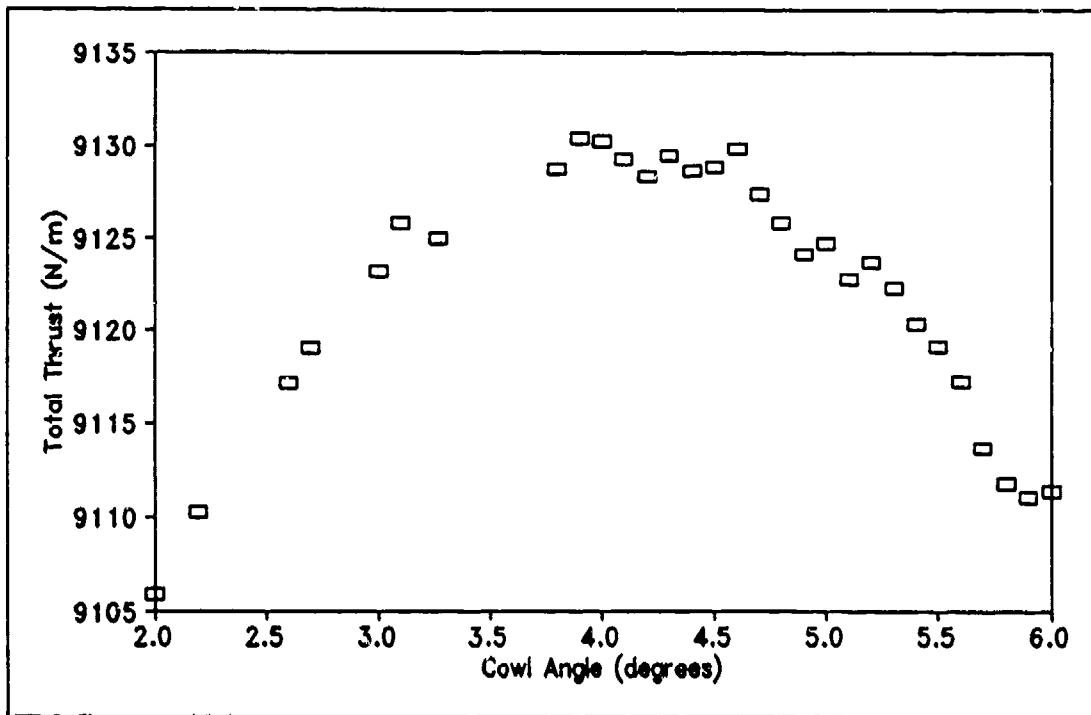
Figure 26. The effect of cowl deflection angle on total wall thrust for Mach number 17.5 and nozzle attachment angle 20.6 degrees.
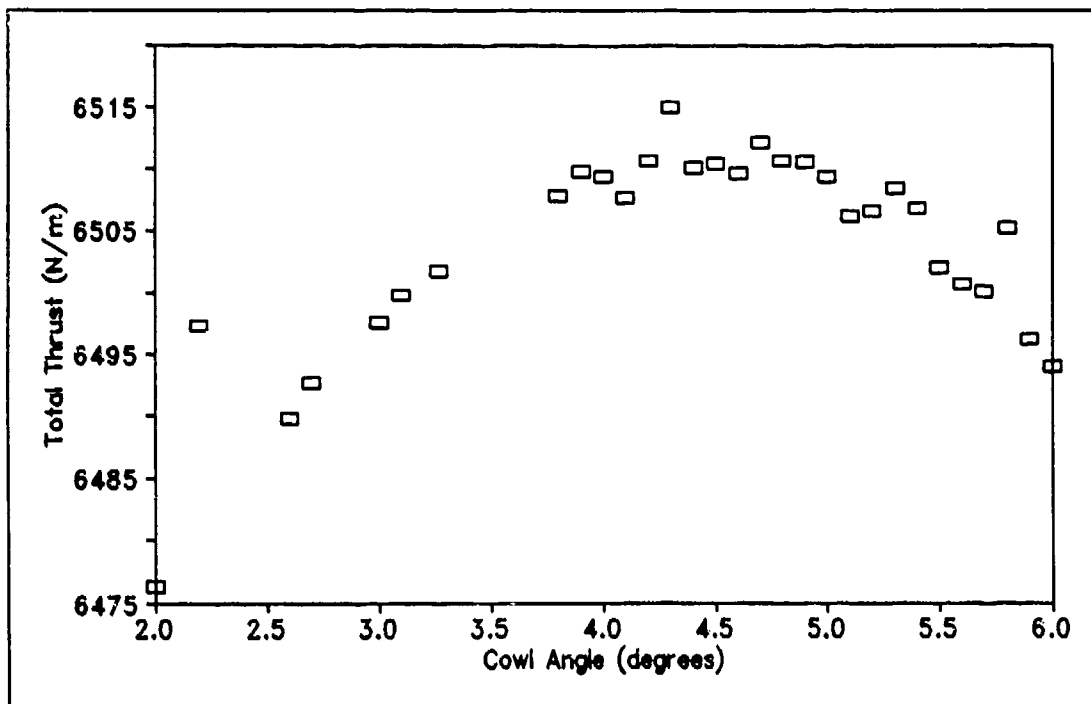
Figure 27. The effect of cowl deflection angle on total wall thrust for Mach number 20.0 and nozzle attachment angle 20.6 degrees.
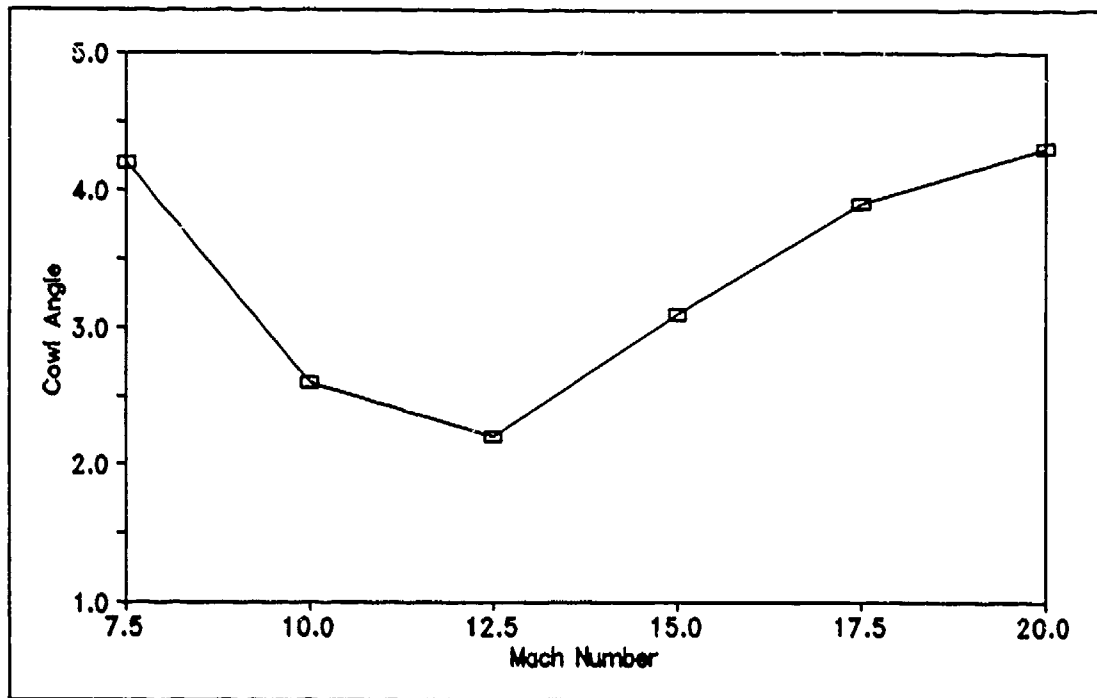
Figure 28. The relationship between Mach number and cowl deflection angle for best off-design performance.
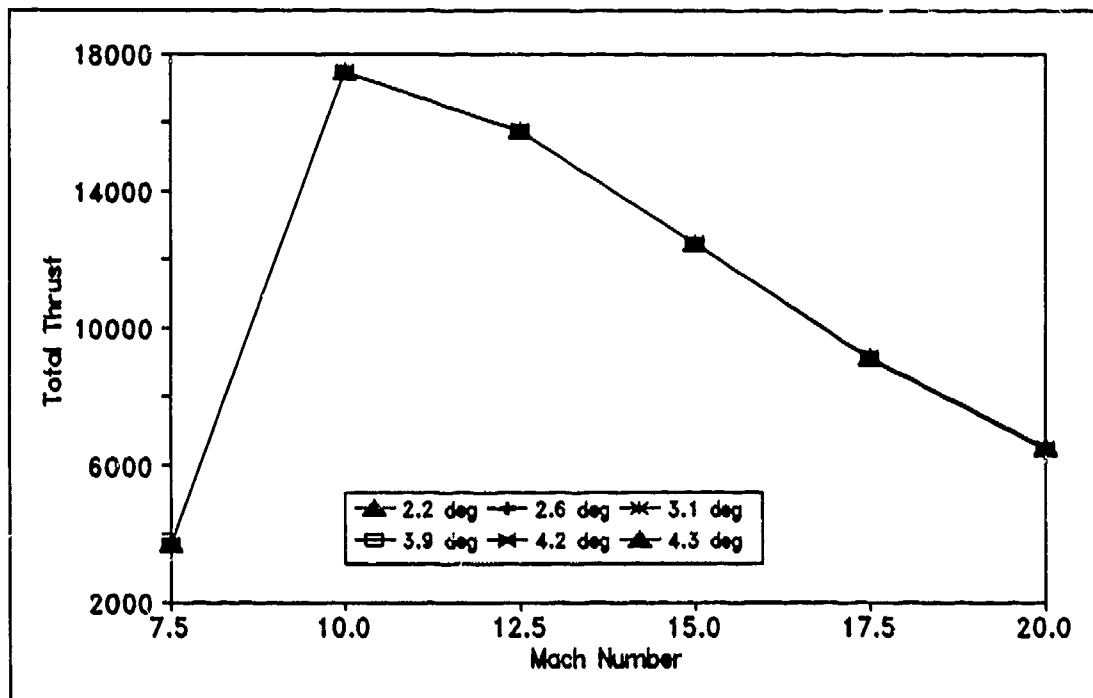
Figure 29. The relationship between total wall thrust and Mach number for various cowl deflection angles and nozzle attachment angle 20.6 degrees.
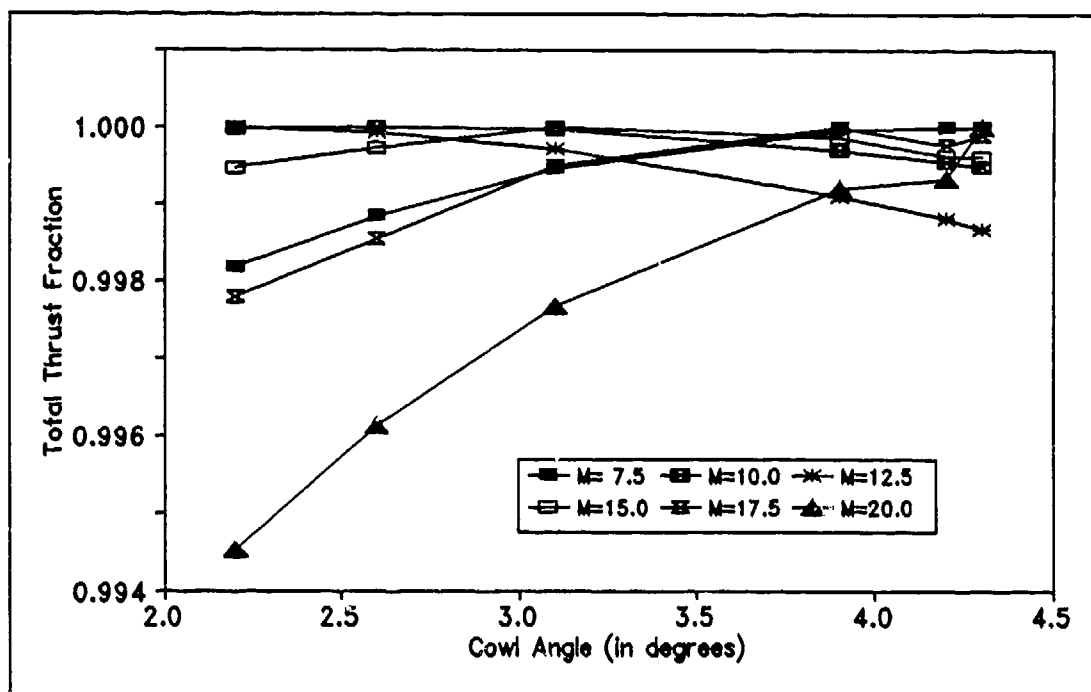
Figure 30. The relationship between total wall thrust fraction and cowl deflection angle for the various points on the trajectory and nozzle attachment angle 20.6 degrees.
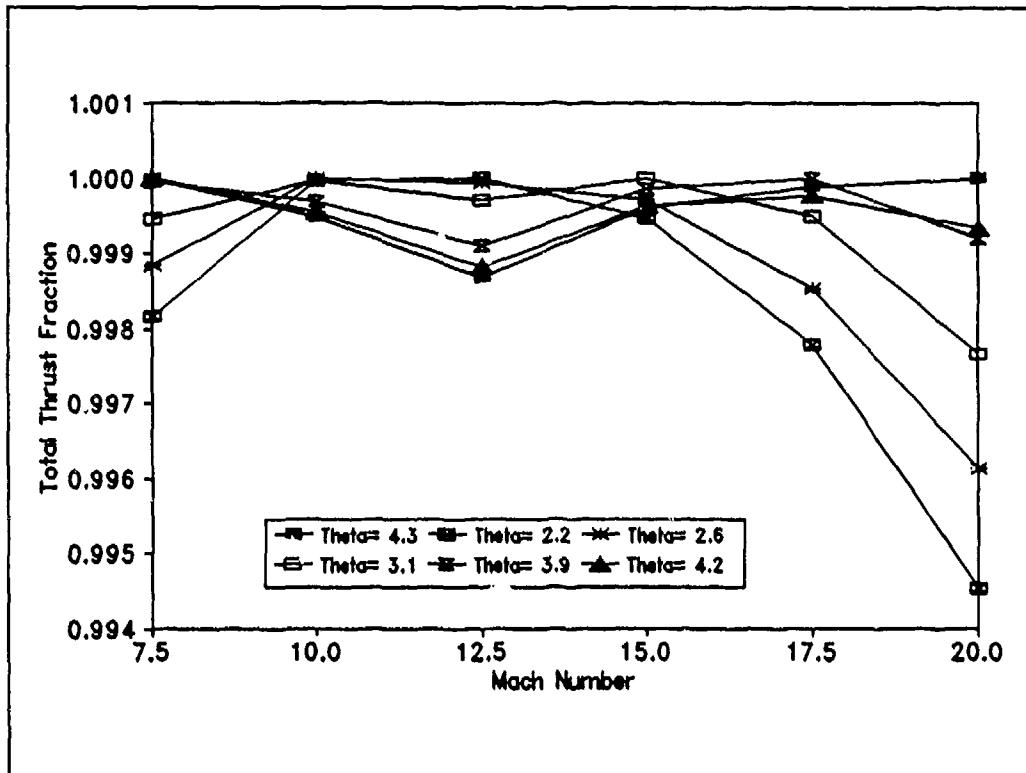
Figure 31. The relatiorship between total wall thrust fraction and Mach number for the various cowl deflection angles and nozzle attachment angle 20.6 degrees.
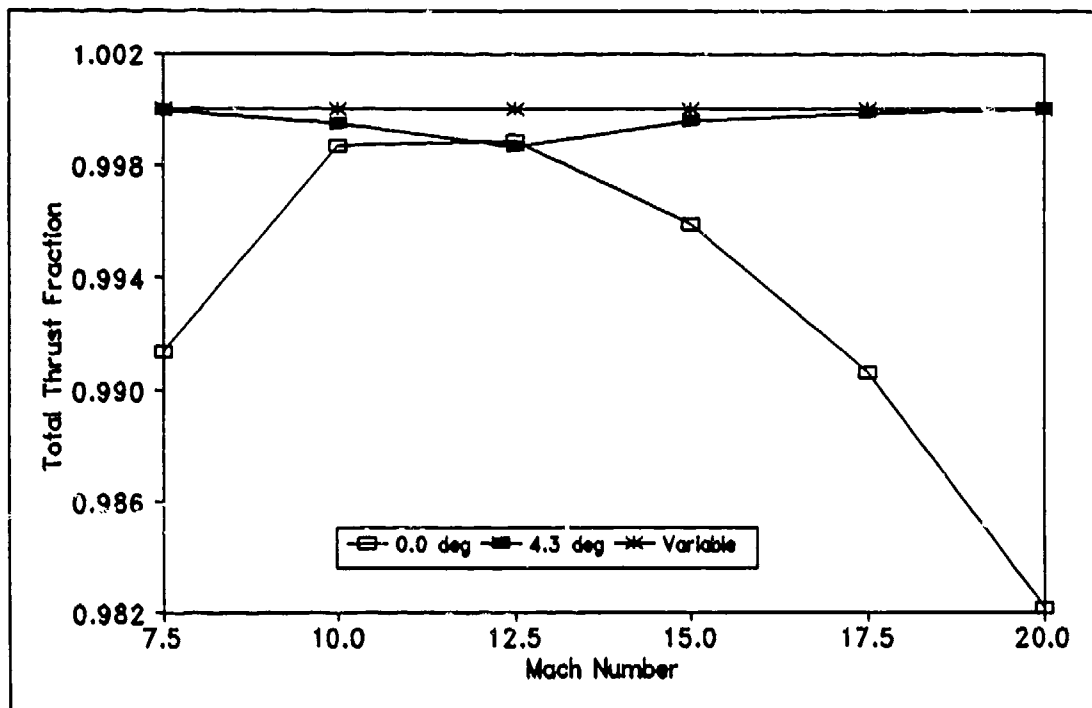
Figure 32. The relationship between total wall thrust fraction and Mach number for three cowl angle cases and nozzle attachment angle 20.6 degrees.

105

Table 5. Geometry for nozzle parametric studies.

Nozzle parameter	Value
length, L (m)	2.54
inlet height, h_{i_1} (m)	0.0254
exit height, h_{i_2} (m)	0.635
circular arc radius of curvature, r (m)	0.0254
circular arc attachment angle, θ_1 (deg)	to be determined
Cowl Parameter	Value
length, xcwl1 (m)	0.254
length, xcwl2 (m)	0.0
thickness, hcwl2 (m)	0.00635
cowl angle, tcwl1 (deg)	0.0
circular arc radius of curvature, rucwl1 (m)	0.0254
cowl taper angle, acwl2 (deg)	10.0

Table 6. Geometry for cowl parametric studies.

Nozzle parameter	Value
length, L (m)	2.54
inlet height, h_{i_s} (m)	0.0254
exit height, h_{e_s} (m)	0.635
circular arc radius of curvature, r (m)	0.0254
circular arc attachment angle, θ_s (deg)	20.6
Cowl Parameter	Value
length, xcwl1 (m)	0.10
length, xcwl2 (m)	0.154
thickness, hcwl2 (m)	0.00635
cowl angle, tcwl1 (deg)	to be determined
circular arc radius of curvature, rucwl1 (m)	0.0254
cowl taper angle, acwl2 (deg)	10.0

Table 7. Nozzle wall thrusts for nozzle optimization study.

Mach number	Nozzle attachment angle (deg)	Nozzle wall thrust (N/m)
7.5	38.000	3866.59
10.0	38.625	18717.63
12.5	30.000	16059.50
15.0	24.600	12351.89
17.5	20.600	8925.91
20.0	17.814	6307.55

Table 8. Nozzle wall thrusts for off-design parametric study.

Nozzle attachment angle	Nozzle wall thrust for Mach number 7.5	Nozzle wall thrust for Mach number 10.0	Nozzle wall thrust for Mach number 12.5
38.000	3866.59	18716.75	15924.30
38.625	3866.32	18717.63	15906.82
30.000	3833.59	18517.65	16059.50
24.600	3745.38	18031.26	15941.20
20.600	3631.72	17332.40	15616.13
17.814	3538.93	16678.50	15164.70

Nozzle attachment angle	Nozzle wall thrust for Mach number 15.0	Nozzle wall thrust for Mach number 17.5	Nozzle wall thrust for Mach number 20.0
38.000	NA	NA	NA
38.625	NA	NA	NA
30.000	12269.61	NA	6100.98
24.600	12351.89	8887.52	6225.61
20.600	12281.45	8925.90	6293.13
17.814	1210(25	8889.74	6307.55

Table 9. Normalized nozzle wall thrusts for off-design parametric studies.

Nozzle attachment angle	Nozzle wall thrust fraction for Mach number 7.5	Nozzle wall thrust fraction for Mach number 10.0	Nozzle wall thrust fraction for Mach number 12.5
38.000	1.00000	0.99995	0.99158
38.625	0.99993	1.00000	0.99049
30.000	0.99146	0.98932	1.00000
24.600	0.96865	0.96333	0.99263
20.600	0.93926	0.92599	0.97239
17.814	0.91526	0.89106	0.94428
13.511	0.86717	0.82616	0.86241

Nozzle attachment angle	Nozzle wall thrust fraction for Mach number 15.0	Nozzle wall thrust fraction for Mach number 17.5	Nozzle wall thrust fraction for Mach number 20.0
38.000	NA	NA	NA
38.625	NA	NA	NA
30.000	0.99334	NA	0.96725
24.600	1.00000	0.99570	0.98701
20.600	0.99430	1.00000	0.99771
17.814	0.97963	0.99595	1.00000
13.511	0.92110	0.96219	0.98530

Table 10.   Total wall thrusts for cowl parametric study.

Mach number	Cowl angle (deg)	Total wall thrust (N/m)
7.5	4.2	3692.82
10.0	2.6	17475.62
12.5	2.2	15751.44
15.0	3.1	12454.40
17.5	3.9	9130.47
20.0	4.3	6514.98

Table 11.   Total wall thrusts for zero cowl deflection.

Mach Number	Cowl Angle (deg)	Total wall thrust (N/M)
7.5	0.0	3660.95
10.0	0.0	17453.23
12.5	0.0	15733.80
15.0	0.0	12404.02
17.5	0.0	9044.95
20.0	0.0	6398.65

Table 12. Total wall thrusts for cowl off-design parametric studies.

Cowl angle (deg)	Total wall thrust for Mach number 7.5	Total wall thrust for Mach number 10.0	Total wall thrust for Mach number 12.5
0.0	3660.95	17453.23	15733.80
2.2	3686.07	17475.23	15751.44
2.6	3688.56	17475.62	15750.42
3.1	3690.81	17475.10	15746.85
3.9	3692.65	17470.30	15737.29
4.2	3692.82	17467.74	15732.82
4.3	3692.78	17466.50	15730.64

Cowl angle (deg)	Total wall thrust for Mach number 15.0	Total wall thrust for Mach number 17.5	Total wall thrust for Mach number 20.0
0.0	12404.02	9044.95	6398.65
2.2	12447.79	9110.29	6479.33
2.6	12450.95	9117.16	6489.74
3.1	12454.40	9125.82	6499.78
3.9	12452.68	9130.47	6509.76
4.2	12449.76	9128.32	6510.63
4.3	12449.52	9129.47	6514.98

Table 13. Normalized total wall thrusts for cowl off-design parametric studies.

Cowl angle (deg)	Total wall thrust fraction for Mach number 7.5	Total wall thrust fraction for Mach number 10.0	Total wall thrust fraction for Mach number 12.5
0.0	0.991369	0.998719	0.998880
2.2	0.998172	0.999978	1.000000
2.6	0.998846	1.000000	0.999935
3.1	0.999457	0.999970	0.999708
3.9	0.999955	0.999696	0.999101
4.2	1.000000	0.999549	0.998818
4.3	0.999989	0.999479	0.998679

Cowl angle (deg)	Total wall thrust fraction for Mach number 15.0	Total wall thrust fraction for Mach number 17.5	Total wall thrust fraction for Mach number 20.0
0.0	0.995954	0.990634	0.982145
2.2	0.999469	0.997790	0.994529
2.6	0.999722	0.998543	0.996127
3.1	1.000000	0.999491	0.997668
3.9	0.999862	1.000000	0.999199
4.2	0.999627	0.999765	0.999332
4.3	0.999608	0.999891	1.000000

112

V   Conclusions and Recommendations

5.1 Conclusions

Using the FDS computer program, the assumed vehicle geometry, and the established flight conditions, the present study has shown that a supersonic nozzle can be optimized for thrust performance for a NASP type vehicle over a typical hypersonic trajectory.

Additionally, this study has demonstrated a single nozzle designed for optimum thrust performance at Mach 17.5 can, for a trajectory that ranges in Mach number from 7.5 to 20.0, maintain nearly optimum thrust performance at the higher Mach numbers while suffering only minor off-design performance losses at the lower Mach numbers. This was accomplished by using a nozzle wall attachment angle of 20.6 degrees with a cowl angle of zero.

After performing a cowl angle parametric analysis on a nozzle with wall attachment angle of 20.6 degrees, it was also demonstrated that losses due to nozzle off-design performance could be recovered by varying the cowl angle setting over the trajectory from 4.2 degrees at Mach number 7.5 to 2.2 degrees at Mach number 12.5 to 4.3 degrees at Mach number 20.0.

Furthermore, this study has shown for a nozzle with wall attachment angle of 20.6 degrees, a cowl angle of 4.3 degrees produces the best recovery of off-design

113

performances losses for a flight Mach number of 20.0.
Additionally, losses due to off-design performance are
minimized for this nozzle-cowl angle configuration over the
Mach number range of 7.5 to 20.0 to the extent that thrust
performance is very close to that which would be achieved
with a variable geometry cowl.

Finally, a true optimization for this nozzle-cowl
configuration would require the simultaneous variation and
optimization of all parameters affecting thrust performance.
Thus, the 4.3 degree cowl angle only produces an optimum for
the nozzle with wall attachment angle 20.6 degrees when
operated at Mach 20. Although little is currently known
about how thrust performance might be further improved if
this multi-parameter optimization were performed, all
evidence indicates that even better thrust performance is
possible. Put simply, all thrust performance determined in
this study could be improved upon.

5.2 Recommendations for Further Study

Although some very useful information was uncovered in
the preceding investigation, there remain many different
areas that require closer scrutiny and further study. What
follows is a brief list of some of the areas that deserve
more attention. This list is by no means definitive.

1. Optimization of Nozzle-Cowl Combination

In the current study a single parameter optimization was performed followed by an off-design parametric analysis. As previously described, the nozzle angle was first optimized at discrete locations over the prescribed trajectory, followed by a parametric analysis of cowl angles at this optimum nozzle angle. From this analysis, all available evidence indicates that even better performance can be derived from an optimization that takes into account the simultaneous variation of both the nozzle and cowl angle. To verify this hypothesis and subsequently determine the optimum nozzle-cowl combination, it is recommended that this type of two parameter optimization study be undertaken.

2. Nozzle Optimization that Considers Pitching Moment Requirements As Well As Thrust Requirements

The present study only considered increased thrust as a figure of merit to determine optimum performance. In reality, a nozzle for a NASP type vehicle would also have to be designed for optimum pitching moment as well. Since the thrust forces from the nozzle may not always produce a resultant that acts through the vehicle's center of gravity, nozzle induced moments could be significant. It is for this reason that it is recommended that a thrust-pitching moment nozzle optimization study be undertaken.

3. Thrust Performance Optimization with External Flow
   Parametrics

Throughout this investigation, only one external flow

compression was considered for each trajectory design point.

This compression was simulated by an oblique shock wave that

was caused by a wedge of 6 degree half angle oriented at a 2

degree angle of attack relative to the freestream flow.

Although this produced results representative enough for

this study, in reality it is quite likely that a hypersonic

vehicle would experience angle of attack perturbations over

the course of its trajectory. For this reason it is

recommended that a study be undertaken to assess the effect

of external flow variation on nozzle thrust optimization.

4. Nozzle and Cowl Analysis Using Different Packing
   Schemes

As described in Section 3.8, the computational grid

packing scheme used for the nozzle optimization was

different from that used in the cowl parametric analysis.

Although this posed no major difficulties for the current

investigation, numerical instabilities narrowed the width of

the Mach number range examined. It is possible that these

instabilities could have been obviated, and a less limited

range of Mach numbers examined had a different packing

scheme been used. It is therefore recommended that a study

be undertaken to perform an nozzle-cowl performance analysis

using various grid packing schemes.

116

Bibliography

Billig, Frederick S. and Van Wie, David M. "Efficiency
    Parameters for Inlets Operating at Hypersonic Speeds,"
    Journal of the American Institute of Aeronautics and
    Astronautics, ISABE 87-7047 XX: 118-130 (1987).

-----. "Combustor Inlet Interaction in Scramjet Engines,"
    AFL Technical Review, 2:1: 118-126 (1990).

Chakravarthy, S. R. Development of Upwind Schemes for the
    Euler Equations. NASA CR-4043. 1987.

Craig, Roger R. and Ortwerth, Paul J. An IBM 7090 Program
    for Calculating the Theoretical Performance of a
    Supersonic Combustion Ramjet Engine. Report for Aero
    Propulsion Laboratory, Aeronautical Systems Division,
    Air Force Systems Command, Wright-Patterson AFB, OH,
    April 1962 (ASRMPR TM 62-16)

Curran, Edward T. and Stull, Frank D. The Potential
    Performance of the Supersonic Combustion Ramjet Engine.
    Report for Aero Propulsion Laboratory, Aeronautical
    Systems Division, Air Force Systems Command,
    Wright-Patterson AFB, OH, May 1963 (ASD-TDR-63-336).

Doty, John H. Maximum Thrust Planar Supersonic Nozzles
    Using A Flux-Difference-Splitting Technique. Ph.D
    Dissertation. School of Engineering, Purdue
    University, West Lafayette IN, August 1991.

Doty, John H. et al. "Optimum Thrust Airframe-Integrated
    Scramjet Nozzles," Seventh National Aero-Space Plane
    Technology Symposium, Paper 83. (Classified
    Proceedings) 1989.

Enquist, B. and Osher, S. "Stable and Entropy Satisfying
    Approximations for Transonic Flow Calculations,"
    Journal of Computational Physics, 3: 176-189 (1981).

Godunov, S. K., (1959), "A Finite-Difference Method for the
    Numerical Computation of Discontinuous Solutions of the
    Equations of Fluid Dynamics," Matematiceskii Sbornik,
    47: 271-290 (1959) also Cornell Aeronautical Laboratory
    translation.

Gordon, Sanford and McBride, Bonnie J. Computer program for Calculation of Complex Chemical Equilibrium Compositions, Rocket Performance, Incident and Reflected Shocks, and Chapman-Jouguet Detonations. NASA Special Publication SP-273. Washington: NASA Scientific and Technical Information Office, 1971.

Henry, John R. and Anderson, Griffin Y. Design Considerations for the Airframe-Integrated Scramjet. NASA Technical Memorandum X-2895. Washington: NASA Science and Technical Information Office, 1973.

Kerrebrock, Jack L. Aircraft Engines and Gas Turbines. Cambridge MA: The MIT Press, 1981.

Lefebvre, Arthur W. Gas Turbine Combustion. Washington: Hampshire Publishing Corporation, 1983.

Mattingly, Jack D. et al. Aircraft Engine Design. New York: American Institute of Aeronautics and Astronautics Inc., (1987).

Osher, S., (1981), "Numerical Solution of Singular Perturbation Problems and Hyperbolic Systems of Conservation Laws," Analytical and Numerical Approaches to Asymptotic Problems in Analysis, North Holland Mathematical Studies No. 47, Edited by S. Axelsson, et al., 179-205, 1981.

Pandolfi, M. "Computation of Steady Supersonic Flows by a Flux-Difference-Splitting Method," Computers and Fluids, 10:1: 37-46 (1985).

Peyret, R. and Taylor, T. D. Computational Methods for Fluid Flow. New York: Springer-Verlag Corp, 112-115 (1983).

Roe, P. L. "The Use of the Riemann Problem in Finite-Difference Schemes," Seventh International Conference on Numerical Methods in Fluid Dynamics, Lecture Notes in Physics (Vol. 141). 354-359. 1981.

Smith, John R. Scramjet Cycle Analysis. Report for Aero Propulsion Laboratory, Aeronautical Systems Division, Air Force Systems Command, Wright-Patterson AFB, OH 15 June 1987

Taylor, T. D. et al. "A Study of Numerical Methods for Solving Viscous and Inviscid Flow Problems," Journal of Computational Physics, 9:5: 99-119 (1972).

United States Committee on Extension to the Standard
    Atmosphere. US Standard Atmosphere, 1962. Washington:
    Government Printing Office, December 1962.

United States Committee on Extension to the Standard
    Atmosphere. US Standard Atmosphere, 1976. Washington:
    Government Printing Office, October 1976.

Van Leer, B. "Towards the Ultimate Conservative Difference
    Scheme I. The Quest for Monotonicity," Proceedings of
    the Third International Conference on Numerical Methods
    in Fluid Dynamics, Lecture Notes in Physics, Volume 18,
    edited by H. Cabannes and R. Teuran. New York:
    Springer-Verlag Corp., 1973.

-----. "Towards the Ultimate Conservative Difference Scheme
    II. Monotonicity and Conservation Combined in a
    Second-Order Accurate Scheme," Journal of Computational
    Physics, 14: 361-370 (1974).

-----. "Towards the Ultimate Conservative Difference Scheme
    III. Upstream Centered Finite-Difference Schemes for
    Ideal Compressible Flow," Journal of Computational
    Physics, 23: 263-275 (1977a).

-----. "Towards the Ultimate Conservative Difference Scheme
    III. A New Approach to Numerical Convection," Journal
    of Computational Physics, 23: 276-299 (1977b).

Van Wie, David M. et al. "NASP Inlet Design and Testing
    Issues," AFL Technical Review, 2:1: 100-109 (1990).

Walton, James T. An Overview of Airframe Integrated
    Scramjet Cycle Components and Flow Features. NASP
    Technical Memorandum 1029. Langley VA: NASA Langley
    Research Center, November 1988.

Zucrow, Maurice J., Hoffman, Joe D. Gas Dynamics (Vol. 1).
    New York: John Wiley and Sons, 1976.

Vita

Captain David J. Herring was born on 9 January 1961 in Baltimore, Maryland. He was graduated from John Adams High School in South Bend, Indiana in 1979. From there he went on to receive an Air Force Reserve Officer Training Corps scholarship to attend the Massachusetts Institute of Technology, where he received the degree of Bachelor of Science in Aeronautics and Astronautics in February 1984. Upon graduation, Captain Herring received a commission in the USAF through the ROTC program, and was assigned to the Air Force Flight Test Center at Edwards AFB, California. While there, he worked in the Airframe Systems Division of the 6520th Test Group as the lead Reliability and Maintainability (R&M) Engineer on the T-46A Next Generation Trainer, the MC-130H Combat Talon II, the CV-22 Osprey, and the AC-130U Gunship programs. During his time at Edwards, in addition to his duties as an R&M engineer, Captain Herring also performed operations support flying duties as a Flight Test Engineer in the T-33, MC-130H, and T-38A aircraft. He continued with these duties until May 1990, when he was accepted into the Air Force Institute of Technology's graduate engineering program in Aeronautical Engineering.

December 1991   Master's Thesis

DESIGN OF AN OPTIMUM THRUST NOZZLE FOR
A TYPICAL HYPERSONIC TRAJECTORY THROUGH
COMPUTATIONAL ANALYSIS

David J. Herring, Captain, USAF

Air Force Institute of Technology
Wright-Patterson AFB, OH 45433-6583   AFIT/GAE/ENY/91D-11

An analysis of a planar supersonic nozzle for a NASP type vehicle was performed with
a computer program that used the new upwind flux difference splitting (FDS) method.
Thrust optimization, off-design performance, and cowl angle parametric analyses were
accomplished, using the FDS code, at six points on a 1000 psf maximum dynamic
pressure trajectory, for the Mach numbers 7.5, 10.0, 12.5, 15.0, 17.5, and 20.0.
Results from the single parameter optimization phase of the study indicated that for
the Mach number range from 7.5 to 20.0, the attachment angles identified as optimum
for the respective trajectory points were 38.0, 38.6, 30.0, 24.6, 20.6, and 17.8.
From this range of angles, the 20.6 degree nozzle was found to produce the minimum
off-design performance losses over the entire trajectory. Using the 20.6 degree
nozzle attachment angle, a cowl angle parametric analysis was performed to determine
the extent to which off-design performance losses could be recovered. Although this
study showed that cowl angles of 4.2, 2.6, 2.2, 3.1, 3.9, and 4.3 degrees were
required at the respective trajectory points to maintain best recovery, nozzle
performance was shown to approach that of a variable geometry cowl for a constant
cowl deflection angle of 4.3 degrees.

Supersonic Nozzle, Flux-Difference-Splitting Method, Optimum   135
Thrust Nozzle, Scramjet Nozzle Optimization, Hypersonic Vehicle

Unclassified   Unclassified   Unclassified   UL

GENERAL INSTRUCTIONS FOR COMPLETING SF 298

The Report Documentation Page (RDP) is used in announcing and cataloging reports. It is important that this information be consistent with the rest of the report, particularly the cover and title page. Instructions for filling in each block of the form follow. It is important to *stay within the lines* to meet *optical scanning requirements*.

Block 1. Agency Use Only (Leave blank).

Block 2. Report Date. Full publication date including day, month, and year, if available (e.g. 1 Jan 88). Must cite at least the year.

Block 3. Type of Report and Dates Covered. State whether report is interim, final, etc. If applicable, enter inclusive report dates (e.g. 10 Jun 87 - 30 Jun 88).

Block 4. Title and Subtitle. A title is taken from the part of the report that provides the most meaningful and complete information. When a report is prepared in more than one volume, repeat the primary title, add volume number, and include subtitle for the specific volume. On classified documents enter the title classification in parentheses.

Block 5. Funding Numbers. To include contract and grant numbers; may include program element number(s), project number(s), task number(s), and work unit number(s). Use the following labels:

C	Contract	**PR**	Project
G	Grant	**TA**	Task
PE	Program Element	**WU**	Work Unit Accession No.

Block 6. Author(s). Name(s) of person(s) responsible for writing the report, performing the research, or credited with the content of the report. If editor or compiler, this should follow the name(s).

Block 7. Performing Organization Name(s) and Address(es). Self-explanatory.

Block 8. Performing Organization Report Number. Enter the unique alphanumeric report number(s) assigned by the organization performing the report.

Block 9. Sponsoring/Monitoring Agency Name(s) and Address(es). Self-explanatory.

Block 10. Sponsoring/Monitoring Agency Report Number. (If known)

Block 11. Supplementary Notes. Enter information not included elsewhere such as: Prepared in cooperation with...; Trans. of...; To be published in.... When a report is revised, include a statement whether the new report supersedes or supplements the older report.

Block 12a. Distribution/Availability Statement. Denotes public availability or limitations. Cite any availability to the public. Enter additional limitations or special markings in all capitals (e.g. NOFORN, REL, ITAR).

DOD	See DoDD 5230.24, "Distribution Statements on Technical Documents."
DOE	See authorities
NASA	See Handbook NHB 2200.2
NTIS	Leave blank

Block 12b. Distribution Code.

DOD	Leave blank
DOE	Enter DOE distribution categories from the Standard Distribution for Unclassified Scientific and Technical Reports.
NASA	Leave blank
NTIS	Leave blank

Block 13. Abstract. Include a brief (Maximum 200 words) factual summary of the most significant information contained in the report.

Block 14. Subject Terms. Keywords or phrases identifying major subjects in the report.

Block 15. Number of Pages. Enter the total number of pages.

Block 16. Price Code. Enter appropriate price code (NTIS only).

Blocks 17. - 19. Security Classifications. Self-explanatory. Enter U.S. Security Classification in accordance with U.S. Security Regulations (i.e., UNCLASSIFIED). If form contains classified information, stamp classification on the top and bottom of the page.

Block 20. Limitation of Abstract. This block must be completed to assign a limitation to the abstract. Enter either UL (unlimited) or SAR (same as report). An entry in this block is necessary if the abstract is to be limited. If blank, the abstract is assumed to be unlimited.